Magma ascent and lava flow field emplacement during the 2018–2021 Fani Maoré deep-submarine eruption insights from lava vesicle textures

Pauline Verdurme, Lucia Gurioli, Oryaëlle Chevrel, Etienne Médard, Carole Berthod, Jean-Christophe Komorowski, Andrew Harris, Fabien Paquet, Cécile Cathalot, Nathalie Feuillet, et al.

Magma ascent and lava flow field emplacement during the 2018–2021 Fani Maoré deep-submarine eruption insights from lava vesicle textures

Pauline Verdurme[a,*], Lucia Gurioli[a], Oryaëlle Chevrel[a,b,c], Etienne Médard[a], Carole Berthod[b,d], Jean-Christophe Komorowski[b], Andrew Harris[a], Fabien Paquet[e], Cécile Cathalot[f], Nathalie Feuillet[b], Elodie Lebas[b], Emmanuel Rinnert[f], Jean-Pierre Donval[f], Isabelle Thinon[e], Christine Deplus[b] and Patrick Bachèlery[a]

[a] Université Clermont Auvergne, CNRS, IRD, OPGC, Laboratoire Magmas et Volcans, F-63000 Clermont-Ferrand, France

[b] Institut de physique du globe de Paris, Université Paris Cité, CNRS, F-75005 Paris, France

[c] Observatoire volcanologique du Piton de la Fournaise, Institut de physique du globe de Paris, 97418, La Plaine des Cafres, France

[d] Observatoire volcanologique et sismologique de la Guadeloupe, Institut de physique du globe de Paris, 97113, Gourbeyre, France

[e] BRGM-French geological survey, 3 avenue Claude Guillemin, BP36009, F-45060 Orléans, Cédex 2, France

[f] Geo-Ocean, UMR 6538 Ifremer, Université de Bretagne Occidentale, CNRS, F-29280, Plouzane, France

* Corresponding author:

E-mail address: pauline.verdurme@uca.fr

ORCID ID #: 0000-0003-1928-0009

Abstract

The 2018–2021 Fani Maoré submarine eruption (offshore of Mayotte, Mozambique Channel) extruded a bulk volume of ~6.5 km^3 of basanite magma onto the seafloor at a depth of 3300 m, with effusion rates ranging from 150–200 m^3/s in the first year of the eruption, to

less than 11 m^3/s in the final months. Six oceanographic campaigns provided a large sample set covering the entire flow field at high spatial and temporal resolution. These samples allow us to precisely track syn-eruptive degassing processes through quantification of textural parameters including porosity, pore connectivity, vesicle number density (N_V) and vesicle size distributions (VSD). Three different textural facies have been distinguished. (1) Vesicular lavas (average porosity of 35%) display unimodal VSDs, high N_V (14–214 mm^{-3}), and small and spherical vesicles. (2) Lavas with intermediate porosities (25%) have scarce small vesicles, VSDs shifted towards larger vesicles, and low N_V (0.2–39 mm^{-3}). (3) Dense lavas with low porosities (14%) display bimodal VSDs distribution, a dominant mode of small vesicles, and low N_V (0–87 mm^{-3}). The early phase of activity (Phase 1, June 2018 – May 2019) built the main edifice and was fed by rapid ascent and closed-system degassing of volatile-rich magma ascending from a deep reservoir to the seafloor (Facies 1). Distal samples collected from lava flows emitted during Phase 2, between June and July 2019, show large and irregular shape vesicles mostly related to bubble growth and coalescence, and outgassing during emplacement (Facies 2). These lavas are interpreted to be emplaced during extension of a lava tube system which began to develop during Phase 1. The final phase (Phase 3, August 2019 – January 2021) was associated with lava effusion located at the northwest lava flow front, 6 km from the summit. Phase 3 involved a more degassed magma due to the increase in the length of the magma pathway (Facies 3). Phase 3 lavas were also extremely outgassed and associated with construction of a new complex lava flow field with tumuli and multiple ephemeral vents (lava breakouts). The heterogeneous textures within the studied samples reflect changing ascent and effusion rates with time, leading to emplacement of lava flows which varied depending on the degree of degassing and effusion rate. We conclude that emplacement of the Fani Maoré large submarine lava flow fields developed through extensive and prolonged tube systems this being supported by the high effusion rates.

Key-words: Submarine eruption, Alkali magmas, Textural characterization, Magma degassing, Lava outgassing, Tube-fed inflation

1. Introduction

Submarine volcanism represents about 75% of volcanic activity on Earth (Crisp, 1984), yet submarine eruptions have rarely been directly observed (Chadwick et al., 2008; Murch et al., 2022). Most of the documented historical submarine eruptions have occurred at mid-ocean ridges (Chadwick et al., 2016). Previous work has focused on estimating effusion rates associated with eruptions at mid-ocean ridges by using the volume of erupted lava and the eruption duration (Caress et al., 2012), lava flow morphology (Gregg and Fink, 1995), and dissolved CO_2 and vesicle characteristics (Chavrit et al., 2014, 2012; Jones et al., 2018; Soule et al., 2012). Unusually gas-rich lavas, also known as "popping rocks", have been sampled at the Mid-Atlantic Ridge (Hekinian et al., 1973; Sarda and Graham, 1990). Such popping rocks are thought to be examples of undegassed magma (Jones et al., 2019; Sarda and Graham, 1990). However, due to limited access, the origin of many submarine magmas, their ascent and degassing history, as well as the emplacement characteristics of lava flows on the ocean floor, remain poorly understood.

The dynamics of magma ascent and degassing have been partly inferred from textural analysis (Blower et al., 2003; Cashman et al., 1994; Shea et al., 2010). In particular, bubbles resulting from exsolution of volatiles in a magma are frozen as vesicles (Colombier et al., 2021; Shea et al., 2010). In subaerial products from explosive basaltic eruptions, characterization of vesicle shape, vesicle size distribution (VSD) and vesicle number density (N_V) have been used to investigate magma ascent and fragmentation in Hawaiian-style fire fountains and Strombolian-style explosive eruptions (e.g., Gurioli et al., 2008). For effusive basaltic

eruptions, textural analysis has been used to aid the understanding of, for example, the transition from pahoehoe to a'a surface texture types (e.g., Polacci et al., 1999), the emplacement dynamics of channel-fed flows (e.g., Harris et al., 2022), and lava flow degassing and outgassing (Cashman et al., 1994; Polacci and Papale, 1997). According to Burgisser and Degruyter (2015), degassing is defined as the general process by which magma loses its volatiles elements by exsolution or outgassing. Whereas outgassing is the physical process by which gas escapes from the magma by bubble rise.

In May 2018, an intense and deep seismic crisis impacted Mayotte Island (north Mozambique Channel) (Feuillet et al., 2021; Lemoine et al., 2020). The seismicity migrated towards the surface at the beginning of June 2018, and the eruption began between June 17 and June 27 (Mercury et al., 2023) and continued for about two and half years. Located ~50 km east of Mayotte, the eruption extruded a bulk volume of around 6.5 km^3 of basanitic magma (Berthod et al., 2021; Feuillet et al., 2021; Lemoine et al., 2020) to create a 820 m high submarine volcano, named Fani Maoré, at a depth of about 3300 m (Feuillet 2019). From June 2018 to May 2019 (Phase 1), Fani Maoré was fed by direct ascent of a basanitic magma from a ~40 km deep reservoir to the surface (Berthod et al., 2021). Between June and July 2019 (Phase 2), a shallower, sub-crustal (17 km deep) tephri-phonolitic magma reservoir became involved and mixed with the less evolved initial magma (Berthod et al., 2021). Then, in August 2019, the location of lava emplacement shifted ~6 km to the northwest of the initial vent (Phase 3a) (**Fig. 1**). Samples collected from October 2020 to January 2021 demonstrate the draining of magma stored in the shallower reservoir, based on petrological and geochemical variations (Phase 3b) (Berthod et al., 2022). For phase 1, the average effusion rate was very high, at least 150–200 m^3/s (Feuillet et al., 2021), then decreased during phases 2 and 3 (Berthod et al., 2021; Peltier et al., 2022, REVOSIMA 2024). The last activity observed at Fani Maoré was on January 2021 (Berthod et al., 2022).

The 2018 – 2021 submarine eruption of Fani Maoré was extremely well monitored with several oceanographic campaigns providing a large number of samples, mostly "popping rocks" (obtained by seafloor dredges and remotely operated vehicle – ROV) (**Fig. 1**) (Rinnert et al., 2021b, 2021a, 2020; Feuillet, 2019; Fouquet and Feuillet, 2019; Jorry, 2019). This high spatial and temporal sampling resolution of the entire lava flow field, allows us to precisely track the textural evolution and degassing processes of the erupted lava flows during the emplacement history of the lava flow field.

In this paper, we present a textural characterization of Fani Maoré's deep submarine lavas. Bulk texture measurements (porosity and vesicle connectivity) and microscopic texture measurements (VSD and N_V), reveal degassing variations in time and space, which we interpret to be due to differing ascent dynamics. Our results enable us to propose eruptive degassing scenarios for magma ascent and lava flow emplacement mechanisms on the seafloor during this eruption.

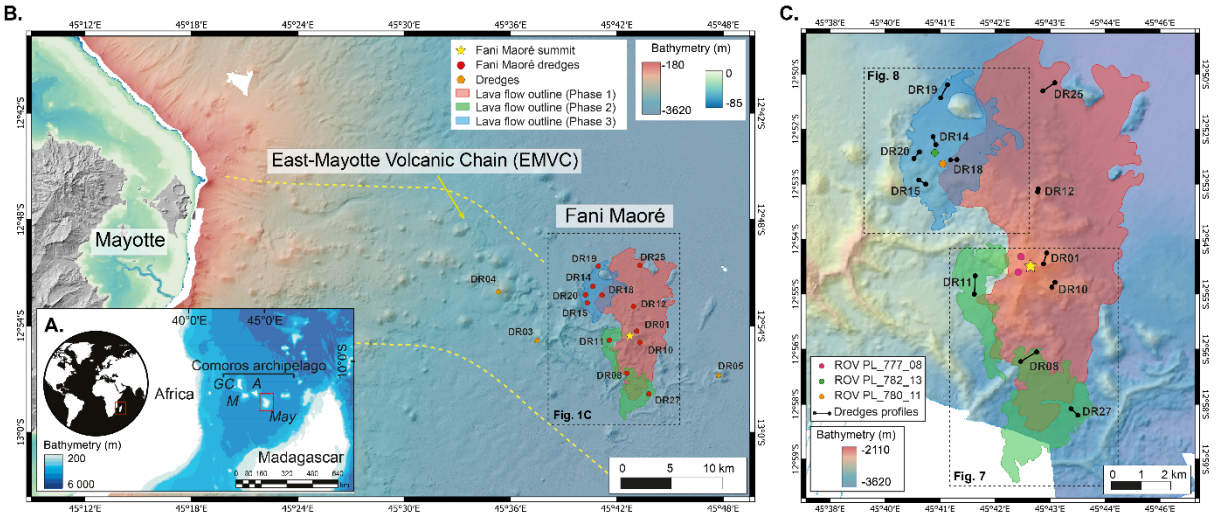

Figure 1. *Location of Fani Maoré volcano (summit shown by yellow star).* **A.** *Simplified map of the Comoros archipelago location showing the four main islands, from east to west: Mayotte (May), Anjouan (A), Mohéli (M) and Grande Comore (GC) (Modified from Berthod et al. (2021))* **B.** *Geological map of the East-Mayotte submarine Volcanic Chain (EMVC) showing the location of the dredges (DR label) used in this study on Fani Maoré and on three other*

unnamed volcanic edifices (DR03, DR04 and DR05). **C.** *Location of the dredges and ROV dives on Fani Maoré lava flows. Lava flow outlines have been modified from Feuillet et al. (2021). Background is the bathymetry from the Homonim project (SHOM, 2016), DEM Litto3D IGN-SHOM (SHOM, 2016) and MAYOBS (Rinnert, 2019).*

2. Methods

2.1. Samples

Rock samples considered here cover the entire 2018 – 2021 Fani Maoré eruption (Berthod et al., 2022, 2021) and were collected at a water depth ranging from 2800 to 3400 m by dredging or using a Remotely Operated Vehicle (ROV). Sampling was carried out during the following oceanographic campaigns: MAYOBS-1 (Feuillet, 2019b), -2 (Jorry, 2019), -4 (Fouquet and Feuillet, 2019), -15 (Rinnert et al., 2020), -21 (Rinnert et al., 2021b) and GeoFLAMME (Rinnert et al., 2021a) (**Table 1**, **Fig. 1**). The observation of an acoustic plume (Feuillet et al., 2021) provides the precise location of Fani Maoré summit and so, the location of all samples in relation to the vent position. Four dredges (DR01, DR10, DR12, and DR25), and one ROV dive (PL_777_08), sampled the area near the summit, as well as the surrounding lava flows emitted during the first phase of the eruption between June 2018 and May 2019 (**Fig. 1**, Berthod et al., 2022). Three dredges (DR08, DR11, and DR27) collected samples from the south and southwest flanks from lava emplaced during Phase 2 between June and July 2019 (**Fig. 1**, Berthod et al., 2022). Finally, five dredges (DR14, DR15, DR18, DR19, and DR20), as well as two ROV dives (PL_780_11 and PL_782_13), sampled lava from the late eruptive phases, to the northwest, between August 2019 and January 2021 (Phases 3a and 3b) (Berthod et al., 2022).

During these campaigns, a dredge operation typically sampled about 400 to 1000 kg of rocks (see Berthod et al. (2022) for the dredging protocol). These rocks were sorted on board

147 to select samples representative of the entire rock diversity, in terms of degree of alteration and
148 morphology. Most dredged samples were metric to decametric pillow lavas, pahoehoe lobes,
149 fragments of lava channel and tube roof, sheet lava and lava pillars. We selected only unaltered
150 and quenched lava selvages within each representative morphology and textural grouping found
151 for each dredge and ROV dive. We measured porosity and connectivity on 100 samples in total
152 (40, 27 and 33 for Phases 1, 2 and 3, respectively), a sufficient number to be statistically
153 representative. From these samples, we selected 17 for more detailed textural analysis (see
154 **Supplementary Material S1** for a full description of each selected sample).

155 We also carried out measurements on submarine basanitic samples from three older
156 edifices of the East-Mayotte submarine Volcanic Chain (EMVC) (DR03, DR04, and DR05,
157 **Fig. 1**). **Supplementary Material Table 1** gives the complete database with all porosity and
158 connectivity measurements, as well as the sample description and chemistry.

159 ***Table 1.*** *Location of the dredges and ROV samples collected during the oceanographic cruises. Latitudes and longitudes are given in degrees*

160 *minutes (DM) and depth in meters (m). Only samples used for the detailed textural analysis are listed here.*

Dredges	Eruptive phase	IGSN number	Samples Name	Samples Name in the text	Oceanographic Campaigns	Start dredging			End dredging		
						Latitude	*Longitude*	*Depth*	*Latitude*	*Longitude*	*Depth*
DR01	1	BFBG-168516	MAY01_DR01_03	DR01	MAYOBS 1	12°54.30'S	45°43.13'E	3050	12°54.51'S	45°43.08'E	2820
DR08	2	BFBG-168595	MAY02_DR08_01	DR08	MAYOBS 2	12°56.46'S	45°42.88'E	3072	12°56.05'S	45°41.91'E	3050
DR10	1	BFBG-168447	MAY04_DR10_02_02	DR10	MAYOBS 4	12°54.94'S	45°43.31'E	3120	12°55.05'S	45°43.24'E	2950
DR11	2	BFBG-168478 -	MAY04_DR11_02_05 MAY04_DR11_07_04	DR11_02_05 DR11_07_04	MAYOBS 4	12°54.80'S	45°41.57'E	3250	12°55.20'S	45°41.55'E	3228
DR12	1	-	MAY04_DR12_02_03	DR12	MAYOBS 4	12°52.90'S	45°42.94'E	3245	12°52.97'S	45°42.93'E	3200
DR14	3a	BFBG-180798	MAY15_DR14_03	DR14	MAYOBS 15	12°51.94'S	45°40.65'E	3240	12°51.94'S	45°40.71'E	3210
DR15	3a	BFBG-180805	MAY15_DR15_02_03	DR15	MAYOBS 15	12°52.71'S	45°40.34'E	3130	12°52.80'S	45°40.49'E	3070
DR18	3b	BFBG-180822	MAY15_DR18_01	DR18	MAYOBS 15	12°52.26'S	45°41.17'E	3270	12°52.27'S	45°41.03'E	3265
DR19	3a	BFBG-180859	GFL_DR19_02	DR19	GeoFLAMME	12°50.63'S	45°40.96'E	3363	12°50.92'S	45°40.81'E	3369
DR20	3b	-	GFL_DR20_02_01	DR20	GeoFLAMME	12°52.09'S	45°40.35'E	3224	12°50.92'S	45°40.81'E	3135
DR25	1	CNRS0000018038	MAY21_DR25_09	DR25	MAYOBS 21	12°50.59'S	45°43.31'E	3478	12°50.77'S	45°43.05'E	3455
DR27	2	CNRS0000018080	MAY21_DR27_04	DR27	MAYOBS 21	12°57.84'S	45°43.81'E	3433	12°57.70'S	45°43.66'E	3431

ROV Dive			Samples Name	Samples Name in the text	Oceanographic Campaigns	Sample location		
						Latitude	*Longitude*	*Depth*
PL_777_08	1	-	GFL_PL777_08_PBT01	PL777_08_PBT01	GeoFLAMME	12°54.39'S	45°42.43'E	2259
		-	GFL_PL777_08_08	PL777_08_08		12°54.14'S	45°42.39'E	2882

161

2.2. Density, porosity and connectivity measurements

Textural and physical measurements (density, porosity and connectivity) were carried out at the Laboratoire Magmas et Volcans (LMV, Université Clermont-Auvergne, France), using the method of Thivet et al. (2020) for density measurements and the strategy developed by Colombier et al. (2017) to measure vesicle connectivity. Dense rock equivalent (DRE) density, skeleton volume of the solid phases and volume of isolated vesicles were obtained using an Accupyc 1340 Helium Pycnometer. In addition, envelope volumes (solids and all vesicles) and bulk density were acquired using a Geopycnometer 1360. All results are given as average values for five measurements per sample (see http://wwwobs.univ-bpclermont.fr/SO/televolc/dynvolc for full description of protocols used for measuring porosity and connectivity).

We carried out measurements of porosity and connectivity on 3 to 15 samples per dredge. These measurements were performed on samples located close to pillow- or flow-selvages and were cut into 4 × 2 cm rectangular blocks. Given that our samples were obtained from the upper sections of the lava flows through dredging, they likely represent the most vesicle-rich portion of the flows.

2.3. Microscopic texture

At least one representative sample from each dredge and ROV dive were prepared as thin sections to allow a more detailed textural analysis. To quantify the petrographic characteristics of each thin section, images were acquired at different magnifications (one image capturing the entire thin section, and up to 10 images at ×25 magnification) following the strategy of Shea et al. (2010). This allowed us to capture the entire vesicle population down to the smallest vesicles of 0.01 mm. Thin sections were imaged using an optical scanner. Images

at ×25 magnification were acquired using a Jeol 5910 LV Scanning Electron Microscope (SEM) in Back-Scattered Electron (BSE) mode with an acceleration voltage of 15 kV and a beam current of 80 µA.

All images were converted into binary images and processed to extract the different phases (crystals and vesicles) using Photoshop®. In some places, vesicle walls were rebuilt to

(i) reconstruct those broken during sample preparation,

(ii) rebuild very thin walls that disappeared during segmentation, and

(iii) disconnect late-stage coalesced vesicles to reestablish the vesicle state prior to sample quench.

Microvesicles related to post-emplacement crystallization associated with slow cooling (i.e., diktytaxitic texture, Walker, 1989) were not considered. Crystals (olivine, magnetite, plagioclase) were distinguished on the SEM images from their different grey scales. The percentage of crystals in the thin sections was quantified to correct the vesicularity values (Shea et al., 2010).

Vesicle size distribution (VSD), cumulative vesicle size distributions (CVSD) and vesicle number density (N_V) were determined using the MATLAB program FOAMS (Fast Object Acquisition and Measurement System; Shea et al. (2010)), by assuming spherical vesicle shapes. Further information on the image processing used to acquire VSD and N_V is presented in Shea et al. (2010).

3. Results

3.1. Macro- to micro-textural features

Dredged samples predominantly consist of centimetric and decametric blocks which exhibit the characteristic morphology of pillow lavas (**Fig. 2**, Berthod et al., 2022). This being a conical shape with a convex glassy surface that converges into a denser core. Pillow fragments

from Phases 1 and 2 generally present a selvage of variable thickness (2 to 3 cm) that is usually quenched, glassy, cracked and microvesiculated (Fig. 2). Below this layer, vesicles are sub-spherical with diameters varying from <1 mm to 1 cm. Irregular shapes of the largest vesicles suggest that coalescence occurred (Fig. 2). This phenomenon tends to increase towards the internal part of the pillow lava, forming large cavities up to 2 – 3 cm in diameter. The distribution of vesicle number and size with depth in the pillow is typical of spongy (s-type) pahoehoe (Walker, 1989). Samples collected in the northwestern part of the flow field (Phases 3a and 3b) are more massive. Though these samples still present an outer glassy selvage of 2 – 3 cm thick, they are characterized by the appearance of prismatic fractures and pipes in the inner part of pillows. These pipes are 4 cm long and 3 – 6 mm wide (see also Berthod et al., 2022), and are similar to pipe-bearing (p-type) pahoehoe (Wilmoth and Walker, 1993).

Thin sections were made exclusively from pillow selvages. SEM images show a broad range of vesicle sizes, from 0.01 to 6.10 mm. Two distinct populations can be distinguished in microscopic observations: large vesicles >2.40 mm in diameter and small vesicles <2.40 mm in diameter. Vesicles smaller than 0.01 mm are considered to be related to crystallization and are not considered in this study. Samples collected close to the Fani Maoré summit are composed of small vesicles (mean size 0.60 mm), which are homogeneously organized and mostly spherical to sub-spherical, thus showing no signs of coalescence (Fig. 2A). In contrast, distal samples from Phases 1 and 2 contain larger vesicles up to 6 mm in diameter (Figs. 2B and C). These larger vesicles have rounded to complex shapes, hence, highlighting evidence of coalescence. (Figs. 2B and C). Samples associated with the last eruptive phase (Phase 3) have the lowest number of vesicles (Fig. 2D).

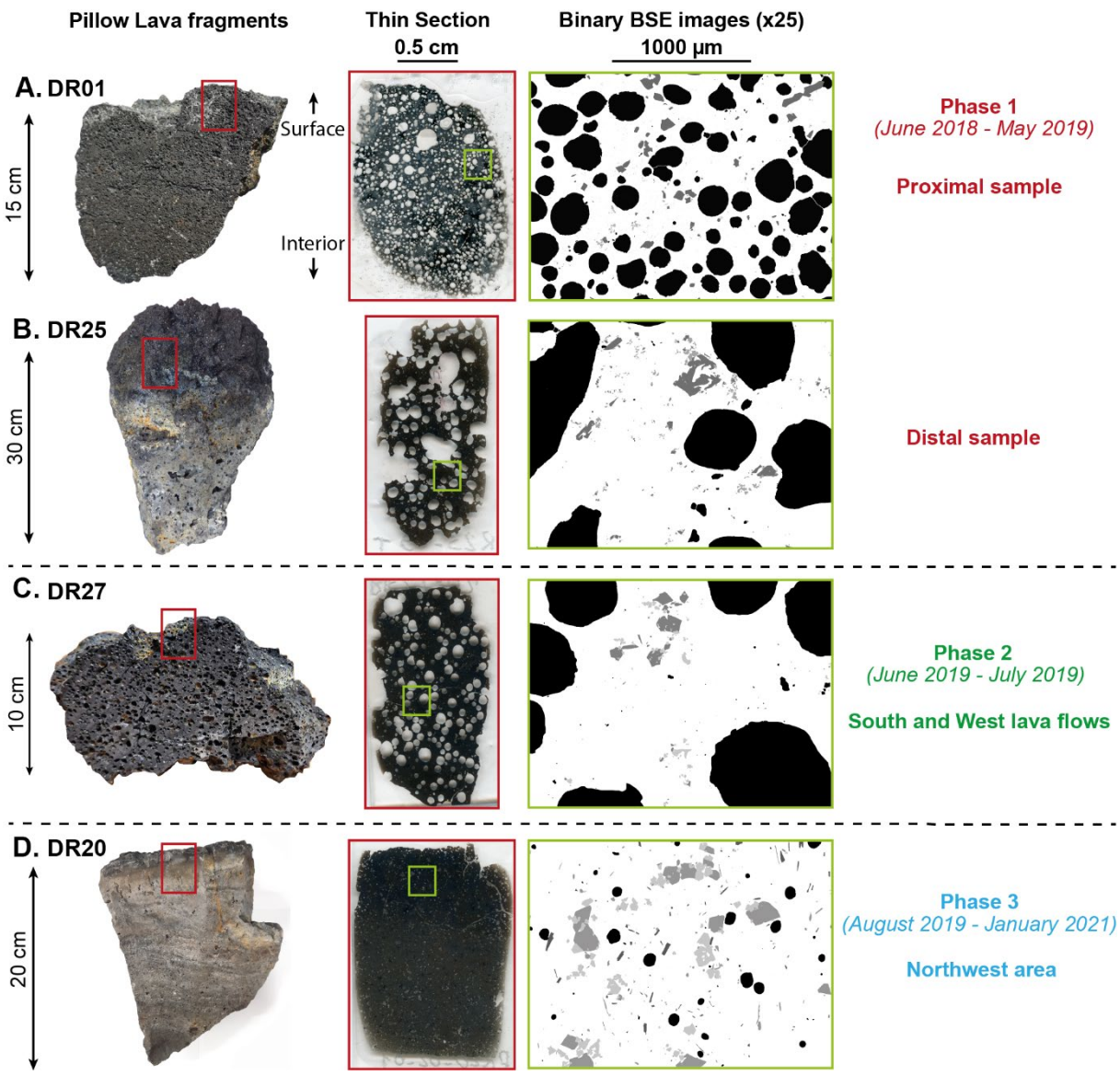

Figure 2. *General textural facies of the pillow lavas from Fani Maoré* ***A.*** *Proximal sample (DR01 - Phase 1),* ***B.*** *Distal sample (DR25 - Phase 1),* ***C.*** *Distal sample (DR27 - Phase 2),* ***D.*** *Sample collected at the northwest area (DR20 - Phase 3). From left to right, picture of a sample section from surface to interior, its associated thin section from the pillow rim, and a binary BSE image (×25) made on the thin section (black = vesicles, white = glass and grey = crystals).*

3.2. Porosity

The bulk porosity (X_t) of the dredged samples shows a decrease over the course of the eruption (Fig 3). During Phase 1, from June 2018 to May 2019, the porosity ranged from 23 to 50%, with an average of 35% (Fig. 3). Distal lava flows emplaced during Phase 2, between

June and July 2019, display a lower bulk porosity between 11 and 41% (average of 25%) (Fig. 3). Over Phase 3, from August 2019 to January 2021, the bulk porosity decreased further to reach values between near zero and 32% (average of 14%). Only DR19, sampled from the extreme distal portion of the Phase 3 lava flow field, shows anomalously low porosity values, ranging from near zero to 4% (Fig. 3).

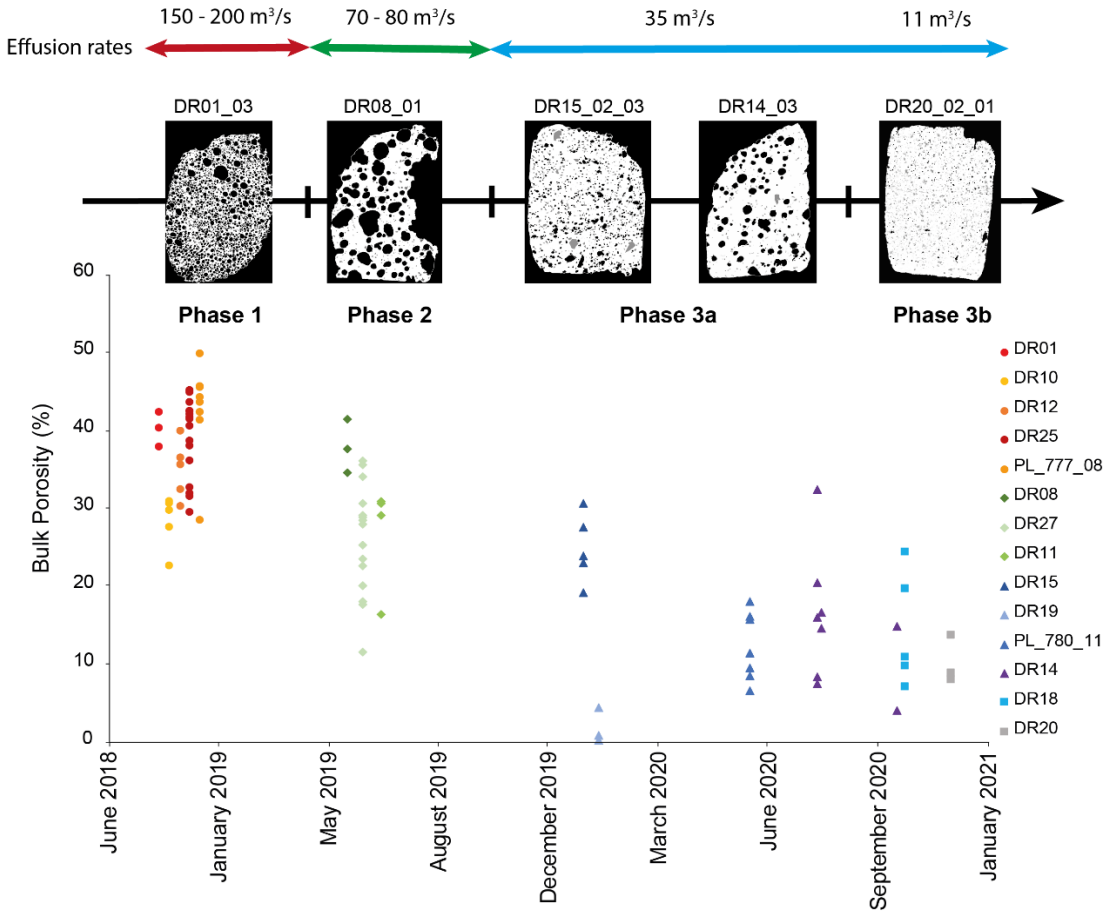

Figure 3. *Bulk porosity (X_t) of the dredged basanite lavas emitted during the 2018–2021 Mayotte eruption at Fani Maoré. Binary images of selected representative samples for each phase is also shown on top to illustrate decrease in porosity over time (black = vesicles, white = glass and grey = crystals). The estimated effusion rates for Phase 1 and for Phases 2 and 3 are taken from Feuillet et al. (2021) and Berthod et al. (2021), Peltier et al. (2022) and REVOSIMA (2024), respectively. Error bars are smaller than the symbol size.*

3.3. Connectivity

The term "pore" includes cracks, vesicles and voids in a rock. Thus, the pore connectivity measurements (C) provide the percentage of connected versus isolated vesicles giving first-order information on the outgassing capacity (Colombier et al., 2017). Our results show that most of the connectivity values are between 0.50 and 1 (**Fig. 4A**), with only a few samples having lower connectivity. This relatively low connectivity recorded in Fani Maoré samples has not been observed on subaerial lava flows (Colombier et al., 2017) and implies the presence of a population of isolated vesicles, which are found throughout the eruption. A few samples are highly connected with connectivity values above one. Such outlying values are likely to be related to extensive fracturing as discussed in Colombier et al. (2017).

Results show that pillow selvages from Phase 1 (DR01, DR10, DR12, DR25 and PL_777_08, **Table 2**) have both a high porosity and a high connectivity ($0.55 < C < 1$). Pillow selvages from Phase 2 (DR08, DR27 and DR11, **Table 2**) maintain a high connectivity ranging from 0.55 to 1, despite having a slightly lower porosity than Phase 1 (**Fig. 4A**). In contrast, the late eruptive stages (Phases 3a and 3b; DR15, DR19, DR14_03, DR18, DR20 and PL_780_11, **Table 2**) have the lowest bulk porosity but cover a broader range of connectivity ($0.20 < C < 1$). These samples appear to be either totally connected ($C = 1$) or have a connectivity restricted to the range 0.80 – 0.20 (**Fig. 4A**).

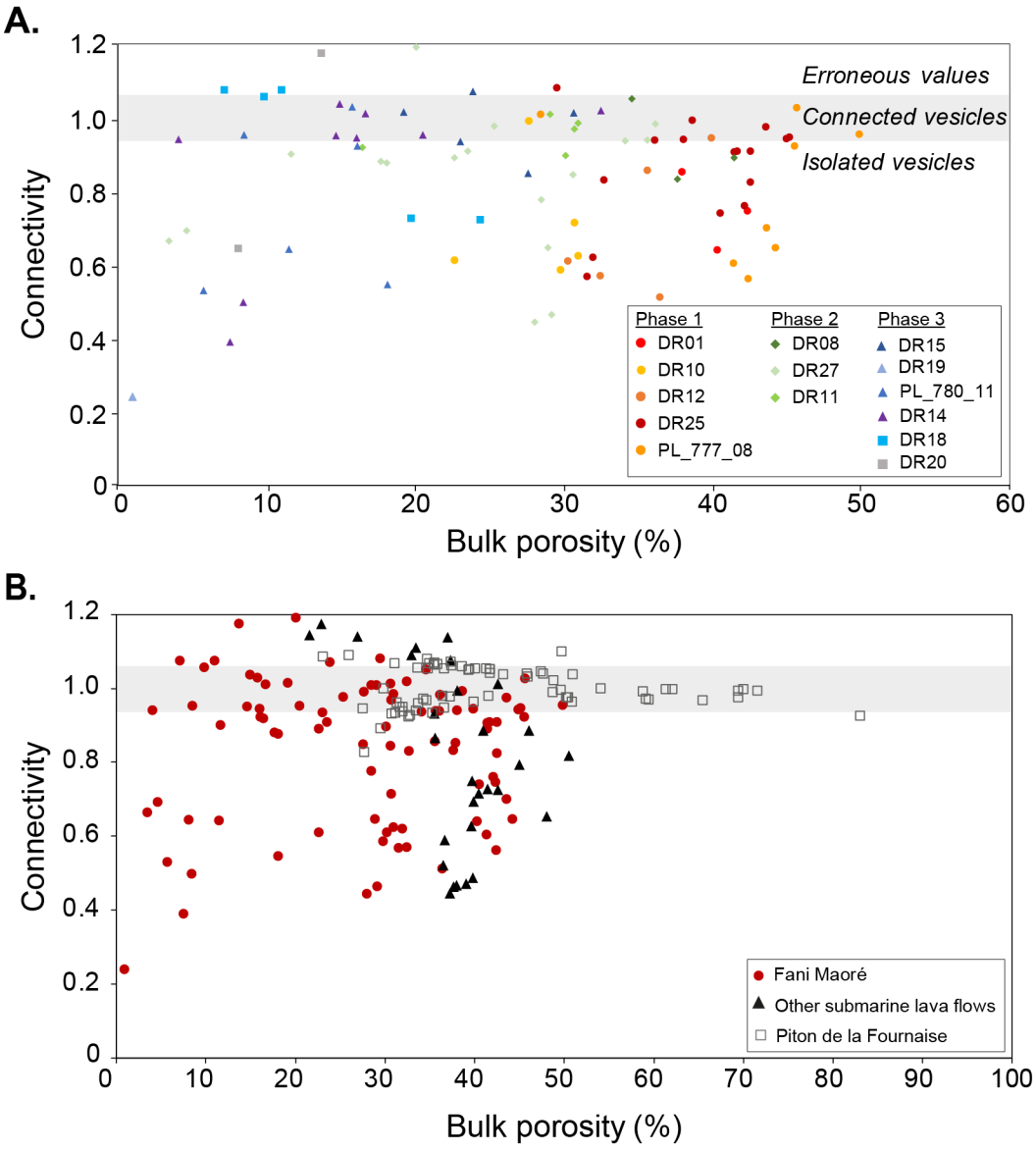

Figure 4. A. *Pore connectivity (C) (expressed as a fraction) versus bulk porosity (X_t) (in percentage). Sample symbols and color code are the same as in Fig. 3. Erroneous values (>1) are unphysical and are likely related to extensive fracturing.* ***B.*** *Comparison between samples presented in this study (red dots, Fani Maoré) and other basanitic samples from volcanic edifices located in the Mayotte submarine chain, DR03, DR04 and DR05 (black triangles, this study) and subaerial basaltic lava flows from Piton de la Fournaise (empty squares, 2015–2016 eruptions after Thivet et al. (2020), 2018–2019 eruptions from Colombier et al. (2021), and 2020–2023 eruptions after Gurioli and Di Muro (2017)).*

3.4. Vesicle characteristics and size distributions

The vesicle size distributions (VSD) (Fig. 5A) and the cumulative vesicle size distributions (CVSD) (Fig. 5B) can be used to infer the processes that may have caused any given distributions (e.g., single or several nucleation events, and continuous nucleation associated with either growth or coalescence) (Shea et al., 2010). Despite having a large range of vesicle sizes, we note that each eruptive phase shows a distinct distribution (Fig. 5).

Most of the samples located near the summit vent (Phase 1) display a unimodal distribution, with vesicles ranging from 0.10 mm to 3.81 mm in diameter, and a main VSD mode at 0.60 mm (Fig. 5-A1). A homogenous population of spherical vesicles associated with a high number of vesicles per unit of area (N_V) mostly characterizes these samples, with values ranging from 14 to 214 mm^{-3}. One distal sample (DR25) has a VSD shifted towards larger and coalesced vesicles (mean size of 2.00 mm) and its N_V declines down to 0.5 mm^{-3} (Table 2), while its porosity remains high (X_t = 36%). The VSDs for samples from Phase 2 mostly show large vesicles with irregular shapes, whose size range (0.96 to 4.77 mm in diameter) coincides approximately with that of distal sample DR25 from Phase 1. However, one sample of DR11 (DR11_02_05) shows a bimodal distribution (Fig. 5-A2), with a second population characterized by smaller vesicles (L: 0.19 to 0.76 mm). Overall, despite a still high porosity (Fig. 3), N_V from Phase 2 is much lower than in Phase 1, ranging from 0.2 to 39 mm^{-3} (Table 2). As for the VSD of the last eruptive phase (Phases 3a and 3b), we also identify a bimodal distribution, with a first population with equivalent diameters (L) of between 0.06 and 0.96 mm, and a second with L from 1.21 to 6.04 mm. As for Phase 1, large vesicles are almost absent in Phase 3 samples and the smallest vesicles are dominant (Fig. 5-A3). However, contrary to Phase 1, vesicles from Phase 3 are the smallest of the dataset with a mean L of 0.30 mm and a low N_V (ranging from 0 to 87 mm^{-3}) (Table 2).

The CVSD distributions for all samples display two distinct trends following either a power or an exponential law indicative of two distinct populations of vesicles (Fig. 5B). If there

is only one population, a power law is expected to continuously decrease towards larger vesicles whereas an exponential law will remain steady at small size of vesicles before dropping sharply (see Shea et al., 2010). Most of the distributions for Phase 1 have a regular trend that obeys a power law for vesicles larger than 1 µm, whereas smaller vesicles deviate from this power law distribution and define an exponential trend (**Fig. 5-B1**). A power law is consistent with a mechanism of continuous nucleation (cf. Cashman et al., 1994), in agreement with the high values of N_V. The same is observed for samples DR11_02_05 (Phase 2) and DR15 (Phase 3a) (**Fig. 5-B2 and B3**, respectively). In contrast, samples lacking small vesicles are characterized by an exponential distribution (**Fig. 5B**) consistent with bubble growth dominated by coalescence (cf. Cashman et al., 1994).

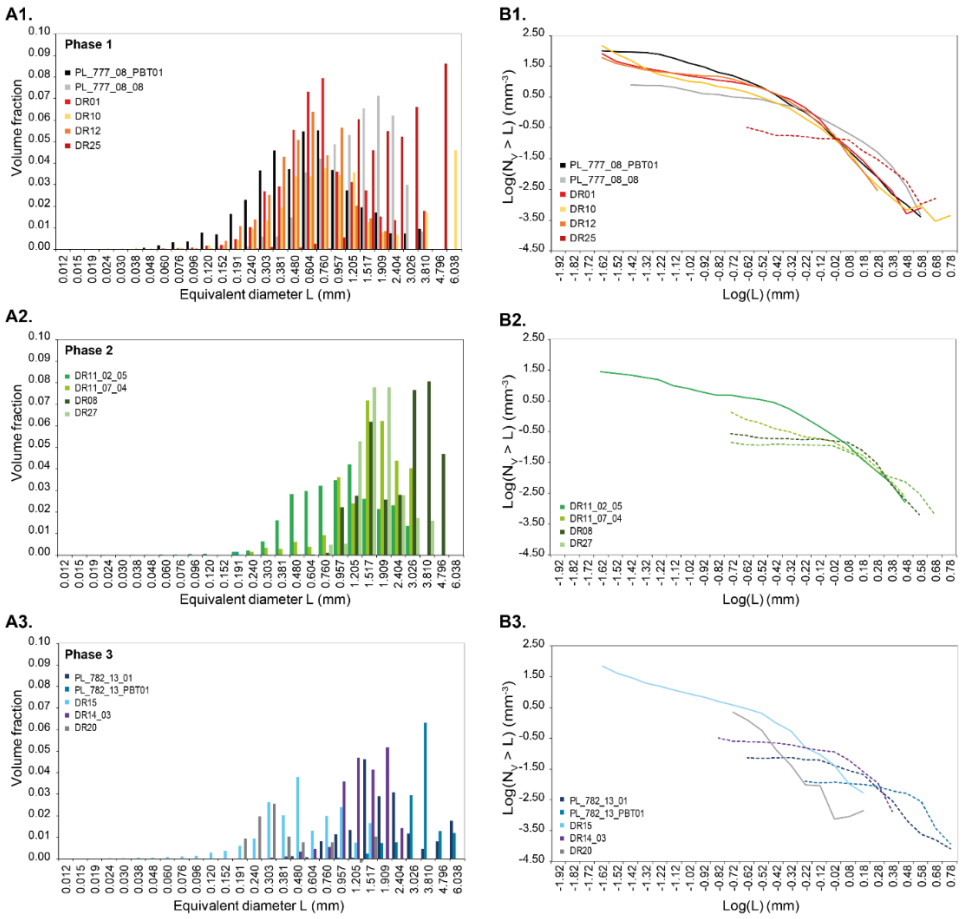

Figure 5. A. *Vesicle size distribution (VSD) and* ***B.*** *Cumulative vesicle size distribution (CVSD) log(N_V > L) vs log(L) for the associated VSD. Solid and dashed lines represent power and exponential law curves, respectively.*

Table 2. *Values for mass and volume of the sample cubes (m_{sample} and V_{sample}), the density of the solid phase (ρ_s), the volume of the solid phase plus the volume of the isolated vesicles ($V_{measured}$), the bulk porosity (X_t), the connectivity (C), the average vesicle diameter (Lmean) and the number of vesicles per unit of area (N_V) of the investigated samples of lava selvages.*

Samples	m_{sample} (g)	V_{sample} (cm^3)	ρ_s (g cm^{-3})	$V_{measured}$ (cm^3)	X_t (%)	C	Lmean (mm)	N_V (mm^{-3})
Phase 1								
GFL_PL777_08_PBT01	29.89 ± 0.01	18.08 ± 0.01	1.65 ± 0.002	13.77 ± 0.054	42	0.56	0.60	184.1
GFL_PL777_08_08	17.95 ± 0.01	11.51 ± 0.01	1.56 ± 0.001	6.12 ± 0.021	45	1.03	1.91	14.0
MAY_DR01_03	15.50 ± 0.01	9.37 ± 0.01	1.65 ± 0.002	6.42 ± 0.018	42	0.74	0.76	142.0
MAY_DR10_02_02	7.61 ± 0.01	3.91 ± 0.02	1.94 ± 0.008	3.06 ± 0.001	31	0.71	0.76	213.9
MAY_DR12_02_03	30.64 ± 0.01	16.51 ± 0.01	1.86 ± 0.001	11.49 ± 0.034	36	0.86	0.60	94.1
MAY_DR25_09	10.74 ± 0.01	5.86 ± 0.00	1.83 ± 0.001	3.87 ± 0.0128	36	0.94	2.40	0.5
Phase 2								
MAY_DR08_01	8.10 ± 0.01	4.64 ± 0.02	1.74 ± 0.008	3.19 ± 0.003	38	0.83	1.20 and 3.81	0.2
MAY_DR27_04	18.96 ± 0.01	9.40 ± 0.01	2.02 ± 0.001	8.23 ± 0.021	28	0.44	1.91	0.4
MAY_DR11_02_05	32.45 ± 0.01	16.51 ± 0.02	1.97 ± 0.002	12.05 ± 0.016	30	0.90	0.96	38.8
MAY_DR11_07_04	17.12 ± 0.01	8.58 ± 0.01	1.99 ± 0.003	6.07 ± 0.005	29	1.01	1.52	2.0
Phase 3								
MAY_DR15_02_03	16.20 ± 0.01	7.19 ± 0.01	2.25 ± 0.003	5.79 ± 0.004	19	1.01	0.48	87.3
GFL_DR19_02	14.06 ± 0.01	5.03 ± 0.02	2.79 ± 0.011	5.02 ± 0.001	<1	0.24	n.a*	n.a
MAY_DR14_03	8.31 ± 0.01	3.52 ± 0.01	2.36 ± 0.009	2.99 ± 0.002	16	0.94	1.52	0.4
GFL_DR18_01	40.21 ± 0.01	15.35 ± 0.02	2.62 ± 0.004	14.17 ± 0.007	7	1.07	n.a	n.a
GFL_DR20_02_01	33.46 ± 0.01	12.91 ± 0.01	2.59 ± 0.001	12.24 ± 0.023	8	0.64	0.30	2.4

**n.a.: not applicable*

4. Discussion

4.1. Porosity and connectivity: comparison with subaerial basaltic lava flows

To compare our results to subaerial deposits we choose the Piton de la Fournaise lava flows because they constitute a unique extensive and solid dataset. Indeed, Piton de la Fournaise volcano produces frequent effusive basaltic eruptions and for the 25 eruptions between 2014 to 2023, porosity and pore connectivity have been measured (Gurioli and Di Muro, 2017). These values are consistent to other subaerial lavas like in Hawaii (e.g.; Harris and Rowland, 2015; Polacci et al., 1999). Several studies have demonstrated that the most vesiculated lava samples are typically located close to the vent (Colombier et al., 2021; Harris et al., 2022; Polacci et al., 1999). Porosity tends to decrease down flow, most likely due to outgassing though local increases in porosity have been observed during slow emplacement and cooling due to coalescence (Cashman et al., 1994; Harris et al., 2022; Walker, 1989). Colombier et al. (2021, 2017) showed that porosity of subaerial basaltic lavas is dominated by total connected porosity, meaning that there are few isolated vesicles, as is also apparent in the texture database for Piton de la Fournaise volcano (Gurioli and Di Muro, 2017; Thivet et al., 2020 – **Fig. 4B**). This has been explained by bubble coalescence during lava transport down a channel (Robert et al., 2014).

If we compare the Piton de la Fournaise dataset to the submarine lavas studied here, we note that our samples have lower porosities of up to 51%, 41% and 32%, for Phases 1, 2 and 3, respectively, and contain a higher number of isolated vesicles, especially in samples from Phase 1 (**Fig. 4B**). A comparison with basanitic samples (DR03, DR04 and DR05) collected at other locations along the EMVC (**Fig. 1**), demonstrates a restricted porosity of less than 50% and low connectivity down to 0.4 (**Fig. 4B**). This confirms that along the entire EMVC it is common to find samples with porosity up to 55%, but submarine lavas can trap a greater number of isolated

vesicles compared to subaerial lavas. This difference between submarine and subaerial samples can be explained by more rapid quenching of the outer layer in contact with water (> 500 °C/s, Thivet et al., 2023b) as opposed to slower quenching due to exposure to the atmosphere (maximum of ~100 °C/s, Hon et al., 1994). This minimizes time for vesicle coalescence, allowing a greater number of vesicles to become locked into the quenched selvage. The rapid quenching of the crust of submarine lava flows thus may help to prevent coalescence, and instead isolates vesicles within the first few centimeters of the lava upper surface in contact with seawater.

When lava interacts with seawater microcracks could form by thermal shock due to rapid quenching (James et al., 2008; Perfit et al., 2003). This would increase pore connectivity. This could also explain the high connectivity, but low coalescence, as observed for a few samples from Phases 3a and b (**Fig. 4A**). Note that whether the Fani Maoré samples were collected close to or distant from the vent, they all had a "popping" behaviour interpreted as being the result of high gas content and rapid stress release during decompression (Sarda and Graham, 1990). This popping behaviour is also driven by rapid expansion of a large number of isolated gas-filled vesicles trapped in the Fani Maoré lavas as evidenced by the strong H_2S smell observed when popping rocks arrived on the ship's deck after dredging.

4.2. Porosity: comparison with other submarine basaltic lavas

In general, submarine lava samples show a restricted porosity range, and two groups can be distinguished (Chavrit et al., 2014, 2012; Dixon et al., 1997; Hekinian et al., 2000; Sarda and Graham, 1990). A first group includes tholeiitic lavas (MORBs) with low porosity ranging between <1% and 5% (Chavrit et al., 2014, 2012), with the exception of popping rocks collected at the Mid-Atlantic Ridge which have vesicularities of up to 17% (Jones et al., 2019; Sarda and Graham, 1990; Soule et al., 2012). A second group includes alkali basalts located at the Mid-

379 Atlantic Ridge with porosities as high as 66 % (Hekinian et al., 2000), and in the North Arch
380 Volcanic Field (Hawaii), at more than 3000 m depth, with porosities of up to 57 % (Dixon et
381 al., 1997). The samples collected at Fani Maoré belong to this second group, as we found
382 porosities as high as 51% (**Fig. 3**).

383 The difference in porosity between MORBs and submarine alkali basalts/basanites may
384 be related to the initial volatile (CO_2, H_2O) contents within the melt. The CO_2 content of
385 MORBs reaches 1 wt.% with a typical dissolved CO_2 in glass of 30 to 400 ppm (Jones et al.,
386 2019; Soule et al., 2012). In addition, MORBs are mostly anhydrous with H_2O contents of <
387 0.4 wt.% (Jones et al., 2019; Sarda and Graham, 1990). Instead, alkali basalts contain up to 5
388 wt.% CO_2 (Buso et al., 2022; Dixon et al., 1997; Hudgins et al., 2015) and ≥1 wt.% of initial
389 H_2O (Buso et al., 2022; Hudgins et al., 2015; Schiavi et al., 2020). In comparison, the pre-
390 eruptive water content for Fani Maoré lavas ranges between 1.2 and 2.3 wt.% with evidence for
391 pre-eruptive CO_2 concentrations possibly up to 1.2 wt.% (Berthod et al., 2021a).

392 In addition to low initial volatile contents, MORBs may experience pre-eruptive bubble
393 loss during crustal storage, so that the regional context may impact the degree of degassing
394 (Chavrit et al., 2012; Graham et al., 2018; Sarda and Graham, 1990). Instead, alkali basalts
395 usually ascend faster with little or no residence time in shallow crustal reservoirs reducing gas
396 segregation and escape (Cooper et al., 2007; Dixon et al., 1997). Petrological studies (Berthod
397 et al., 2021) coupled with seismic data (Feuillet et al., 2021; Lemoine et al., 2020; Mercury et
398 al., 2023) suggest that the basanitic magma that fed Fani Maoré ascended directly from a deep
399 reservoir (~40 km) during Phase 1 therefore minimizing any pre-eruptive outgassing (Berthod
400 et al., 2021). Assuming that vesicle characteristics measured within the lavas collected near the
401 summit vent (sample PL_777_08_PBT01) have undergone minor bubble loss, magma ascent
402 rates can be estimated using the model of Toramaru (2006) based on N_V values. This calculation
403 gives a decompression rate of around 0.09 MPa/s and an ascent velocity of ~3.0 m/s

(**Supplementary Material S2**). However, this estimate considers that bubbles only contain H_2O, but they will also contain some CO_2 (Thivet et al., 2023a). Assuming that the effect of CO_2 dominates over H_2O, and that the saturation pressure occurs at the source depth of around 40 km, we can roughly estimate the ascent rates by substituting H_2O parameters with those for CO_2 (e.g., surface tension and diffusivity after Sarda and Graham (1990) and Watson et al. (1982), respectively). This gives higher magma ascent rates of >10 m/s, an unrealistic value that however suggests that the ascent rates determined from CO_2 alone is a minimum bound. Further work is needed to better understand the role of CO_2 during magma ascent to the seafloor. However, our minimum bound is still higher than those found for MORBs based on CO_2 degassing for the 2011 Axial Seamount eruption which range from 0.02 to 1.2 m/s (Jones et al., 2018). We conclude that the high porosity recorded within our Fani Maoré samples is related to a high initial volatile content (1.2 – 2.3 wt.% H_2O ; 0.6 – 1.2 wt.% CO_2, Berthod et al., 2021a) coupled with fast magma ascent (>3 m/s).

4.3. Implications for lava flow emplacement at Fani Maoré

4.3.1. Phase 1 (June 2018 – May 2019): main lava cone building stage

Deep seismicity (up to a depth of 50 km, Feuillet et al., 2021; Lemoine et al., 2020; Mercury et al., 2023), coupled with petrological studies (Berthod et al., 2021), have revealed the source to be a deep magmatic reservoir at ~40 km. From the source, migration of earthquakes revealed magma ascent towards the southeast. Ascent rates of >3 m/s prevented interaction with shallower and more evolved reservoirs, and resulted in very high effusion rates (150–200 m^3/s, Feuillet et al., 2021). Note that the eruptive style of the very early phases of the eruption cannot be known because the flows from those phases were buried by successive flows by the time of the first observations. Thus, our discussion of Phase 1 only applies to processes occurring once the flow field was well-developed and mature.

429 The high porosity (max. 51 %) and the large number of vesicles per unit area (max N_V
430 = 214 mm^{-3}) recorded in the pillow lavas near the summit vent, suggest that a high content of
431 volatiles had degassed during magma decompression in a nearly closed-system between the
432 deep reservoir and the seafloor. The unimodal VSD implies that one stage of nucleation and
433 bubble growth occurred during magma ascent, with no perturbations due to coalescence or
434 bubble loss (Blower et al., 2003; Giachetti et al., 2010; Mourtada-Bonnefoi and Laporte, 2004;
435 Shea et al., 2010). The homogenous spatial distribution of the vesicles in the samples collected
436 near the vent is consistent with an overall, rather than a local, bubble nucleation mechanism (cf.
437 Le Gall and Pichavant, 2016a). Basanitic compositions may contain up to 5 wt.% of CO_2 (e.g.,
438 Buso et al., 2022) and more than 1 wt.% of H_2O (Buso et al., 2022; Dixon et al., 1997; Head et
439 al., 2011; Hudgins et al., 2015). Decompression experiments have demonstrated that
440 vesiculation in CO_2-bearing melts is caused by a single continuous mechanism of nucleation
441 along the decompression path (Le Gall and Pichavant, 2016a; Yoshimura, 2015). Due to the
442 equilibrium between H_2O – CO_2 fluid and melt, when pressure decreases it induces initial
443 nucleation of CO_2-rich bubbles followed by growth mostly due to water diffusion (Le Gall and
444 Pichavant, 2016a, 2016b). Given an exsolution depth of around 40 km, coupled with very fast
445 magma ascent, there would have been insufficient time for volatile diffusion into existing
446 bubbles, which limited bubble growth and thus their sizes. The very fast ascent rates also
447 prevented any form of coalescence and minimized outgassing prior to eruption.

448 Although proximal samples have a texture related to degassing by exsolution, samples
449 collected at the distal front of the Phase 1 lava flow field (DR25) display a different texture,
450 which indicates outgassing (**Fig. 6**). Even though they retain a high porosity, they are
451 characterized by a much lower N_V (0.5 mm^{-3}) as well as a shift towards larger vesicles as
452 observed in the VSD trend (**Fig. 5**). This can be explained by coalescence of bubbles (cf. Shea
453 et al., 2010). The eruption involved relatively low viscosity (~300 Pa.s) magma (Verdurme et

al., 2023). This would favor coalescence and outgassing during lava flow emplacement on the seafloor (**Fig. 6**), as often observed for subaerial basaltic lava flows (Blower et al., 2003; Cashman et al., 1994; Harris et al., 2022; Polacci et al., 1999). Phase 1 lava reached a distance of about 9 km from the vent to the north of the summit. The flow field morphology and dredged samples of lava tube roofs indicate that lava tubes were established to feed inflated pahoehoe sheet flows to great distances from the vent. Subaerial tube roofs are known to provide very effective insulation reducing heat losses and cooling rates to ≤1 °C/km (Keszthelyi, 1995). In lava tubes, greater distances of flow advancement can be achieved (Keszthelyi, 1995), and complex tube systems can develop during long-lived eruptions to feed distal zones of inflated pahoehoe lava flows (Mattox et al., 1993). Similar complex systems of lava tubes have also been observed at the East Pacific rise (Fornari, 1986). Here, we interpret that lava was transported through a network of lava tubes feeding inflated pahoehoe with long cooling times (cf. Hon et al. 1994) so that outgassing occurred.

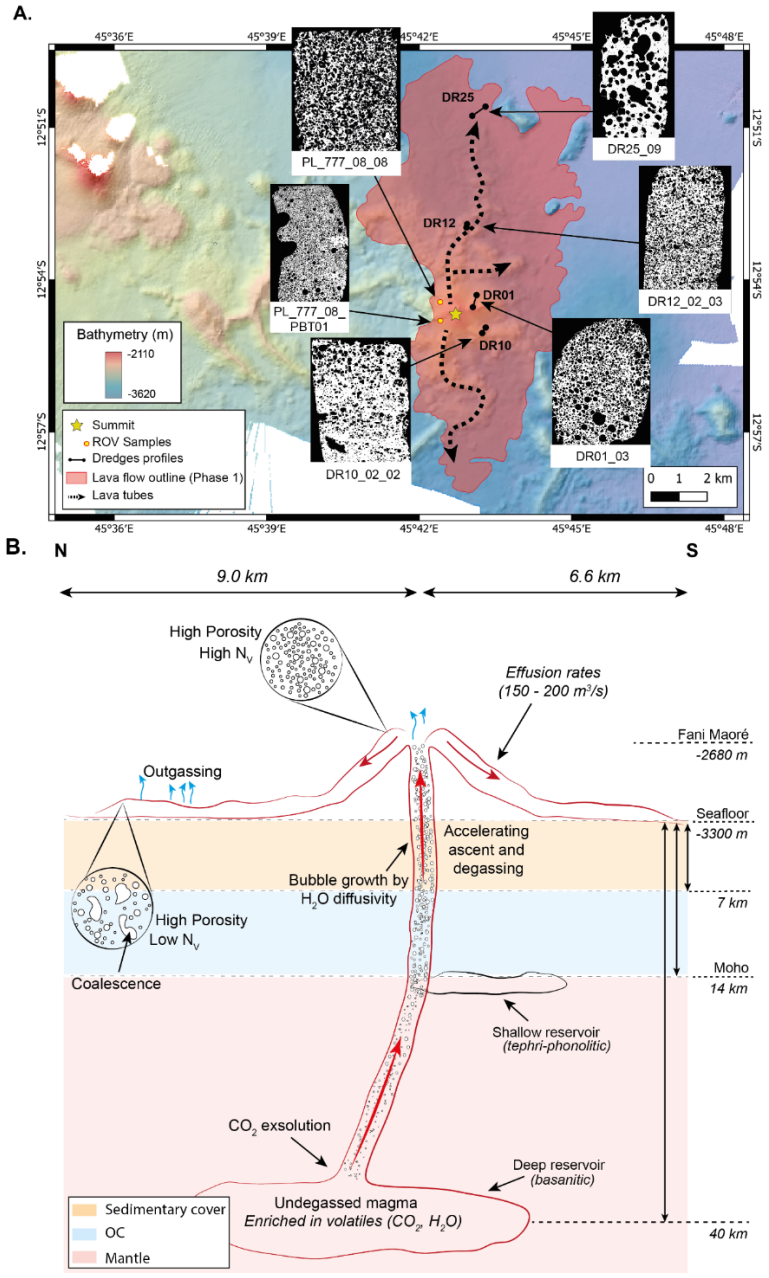

Figure 6. A. *Geological map outlining the lava flow field emitted during Phase 1, from June 2018 to May 2019, on MAYOBS bathymetry (Rinnert, 2019). Binary images of selected thin sections of lava samples are also shown at different locations on the lava flow field.* ***B.*** *Schematic drawing (not to scale) illustrating the dynamics of degassing processes from the magma reservoir to lava flow emplacement on the seafloor. The depths of layers, such as the top of the Mesozoic Oceanic Crust (OC) and the seismic Moho discontinuity, are defined by refraction and reflection seismic data under Fani Maoré in Masquelet et al. (2022, 2023 submitted Tectonophysics).*

476

477 **4.3.2. Phase 2 (June – July 2019): southern and western lava flow fields**

478 Phase 2 lavas are dominated by large vesicles with irregular shapes and N_V ranging
479 between 0.2 and 39 mm^{-3} (**Figs 2 and 5**). Porosities are slightly lower than for Phase 1,
480 indicating that bubble coalescence dominated over nucleation (cf. Blower et al., 2003; Giachetti
481 et al., 2010). Phase 2 samples contain zoned olivine crystals, which suggests that instead of
482 ascending directly from the deep reservoir, the magma interacted with a shallower tephri-
483 phonolitic reservoir at a depth of around 17 km below the seafloor (**Fig. 7**) (Berthod et al., 2022,
484 2021). Given that the ascent rate from the shallow reservoir was slower (minimum 0.005 m/s,
485 Berthod et al., 2021), the effusion rates are also lower (70 – 80 m^3/s, Berthod et al. 2021;
486 REVOSIMA, 2024). Vesicle characteristics are similar to the samples collected at the distal
487 flow front of the Phase 1 lava flow field. This means that more efficient outgassing occurred
488 during magma ascent and lava flow emplacement during Phase 2 (**Fig. 7**).

489 Berthod et al. (2022, 2021) suggested that Phase 2 was emitted by new vents located
490 between ~1 and ~4 km from the Phase 1 vent. However, mapping using bathymetry data
491 indicate that the Phase 2 lava flow field is continuous with that of Phase 1: the former extending
492 from the front of the latter (**Fig. 7A**). The first Phase 2 lava flow field was emplaced from the
493 southern edge of the Phase 1 field in June 2019, and the second was emplaced from the
494 southwest edge of the Phase 1 field in July 2019. This suggests that the main primary vent
495 remained in the same location, but that extension of the flow field in Phase 2 resulted from the
496 establishment of a stable tube system in the Phase 1 flow field, breakouts from the Phase 1 flow
497 front, and extension of the tube system through the Phase 2 flow field (cf. Mattox et al. 1993).
498 The presence of zoned crystals in Phase 2 samples can be explained by a decrease in the magma
499 ascent rate, facilitating interaction with the shallower tephri-phonolitic reservoir as suggested
500 by Berthod et al. (2021) (**Fig. 7B**).

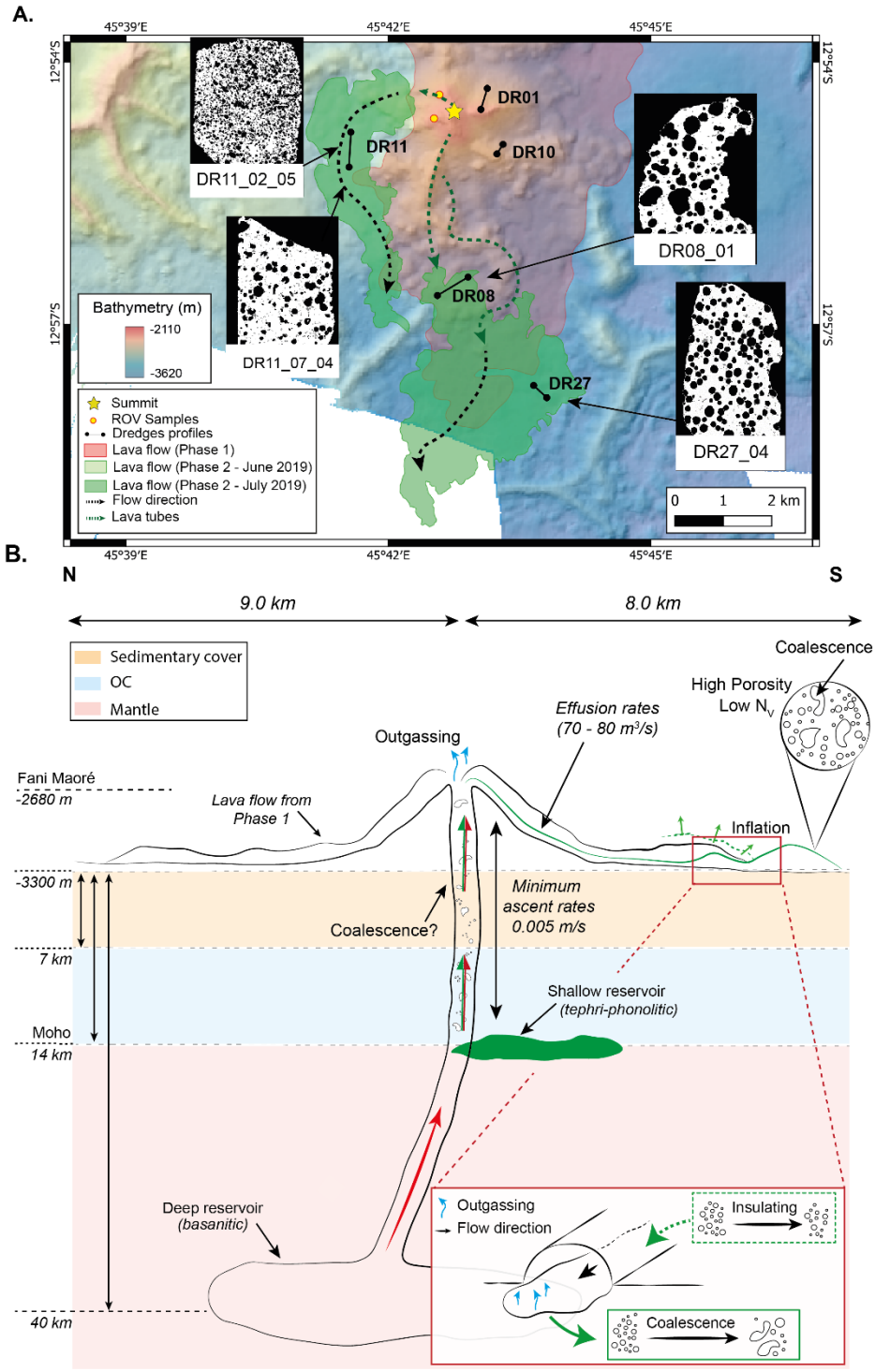

Figure 7. A. *Geological map outlining the lava flows emplaced during Phase 2, from June to July 2019, on MAYOBS bathymetry (Rinnert, 2019). Binary images of selected thin sections of lava samples are also shown at different locations on the lava flows.* ***B.*** *Caption same as* ***Fig. 6****. Bi-color (red and green) arrows represent the interaction between the basanitic and tephri-phonolitic melts.*

507

508 **4.3.3. Phase 3 (August 2019 – January 2021): Northwestern flow field**

509 Phase 3a and b lavas were emitted from a new area 6 km northwest of the main edifice
510 (**Fig. 1**; Berthod et al., 2022). Based on petrological data, Berthod et al. (2022) explains this
511 change in location via a new dyke pathway occurring in the crust above the shallower reservoir.
512 However, the location of Phase 3 lava flows at the periphery of the existing flow field as well
513 as the lack of seismic signal between a depth of around 20 km and the seafloor (e.g., Lavayssière
514 and Retailleau, 2023), although shallow seismicity is also absent below Fani Maoré summit,
515 may also suggest that this new location is likely associated with the breakouts of the Phase 1
516 lava flow front, similarly to Phase 2. Such breakouts, also called ephemeral vents are commonly
517 found in lava flow field with well-established tube system (Calvari and Pinkerton, 1998; Polacci
518 and Papale 1997).

519 Emplacement of the Phase 3 lava flows began around 21 August 2019 and a complex
520 succession of lava flows piled up around a first ephemeral vent (Berthod et al., 2022; Rinnert
521 et al., 2021a, 2020) (**Fig. 8A**). This emission source was most likely close to the location of the
522 DR15 dredge, where bathymetry shows a lava flow field thickness of up to ~ 250 m. The lava
523 flow field extends towards the North. Proximal samples from Phase 3 (DR15) have a higher
524 porosity and N_V (87.3 mm^{-3}) than distal vesicle-free samples (DR19) (**Fig. 8A**). This suggests
525 that an initially degassed magma became outgassed, with crystallization and outgassing
526 occurring during lava flow emplacement under the lower effusion rate conditions (11 m^3/s,
527 Peltier et al. 2022; REVOSIMA, 2024). The anomalously low porosity and high density of
528 DR19 samples can be explained by the location of the dredge at the flow front.

529 Between 10 May and 10 October 2020, a large 760 m long by 450 m wide tumulus-like
530 structure with a well-developed axial cleft 620 m long and about 50 m wide (cf. Walker, 1991)
531 and a height of 40 m developed in the Phase 3a flow field. After it formed, the tumulus emitted

a lava flow from its central cleft and from collapse breakouts at its southern side (Fig. 8B). Between 10 and 22 October 2020, lava flows of Phase 3b erupted in the vicinity of the tumulus, covering it and extending radially away from it (Fig. 8C). This mimics processes observed at active inflating subaerial pahoehoe lava flow fields (e.g., Hon et al. 1994; Mattox et al. 1993; Walker, 1991). Dredge DR14 sampled lava flows from both Phases 3a and 3b, whereas DR18 (Rinnert et al., 2020) only sampled Phase 3b, including thin elongated lava flows, probably fed by tubes emanating from the tumulus structure and its southern flank breakout. Near the tumulus (DR14), we found two types of samples, the first resembling s-type pahoehoe with high porosities (max. 32 %), and the second resembling p-type pahoehoe with low porosities and pipes (Walker, 1989). In contrast, at the distal site (DR18) only p-type pahoehoe with very low porosities are found (Fig. 8C). The texture of Phase 3b samples highlight, again, that magma arriving at the surface experienced a degree of degassing and crystallization during ascent prior to emplacement. This was followed by variable degrees of outgassing during lava flow emplacement and inflation.

The final stage of Phase 3b, from 22 October 2020 to January 2021 was sampled by dredge DR20 (Rinnert et al., 2021a), and was characterized by highly degassed lavas found at five different locations (Fig. 8D). These locations were distributed radially around the southern sector of the Phase 3b tumulus. Samples are of vesicle-poor lava, reflecting degassed magma arriving at the surface. These samples also contain pipes. This texture is consistent with the breakout of outgassed pahoehoe at the end of the inflation phase. We envision this as similar to the previously documented example of the waning phases of lava flow field inflation at Kilauea where ooze out of outgassed spiney and blue glassy pahoehoe previously stored in the flow field was observed around the margins of an inflated flow (e.g., Harris et al., 2007; Rowland and Walker, 1990).

Overall Phase 3 samples are characterized by low porosities (average of 14%), which may be related to decreasing driving pressure at the end of the eruption (cf. Gudmundsson, 2002; Rivalta et al., 2005; Taisne and Jaupart, 2009) when the magma had more time to undergo degassing during ascent (e.g., Jones et al., 2018). Furthermore, depletion of the initial volatile content over the almost two years of eruption prior to Phase 3, may have also resulted in lower porosity. In addition, extended residence time of lava within the flow field could lead to high degrees of outgassing and the emplacement of vesicle poor lava types. Despite generally low porosities, heterogeneous textures within the samples reflect the complexity of the emplacement style of lavas in this area.

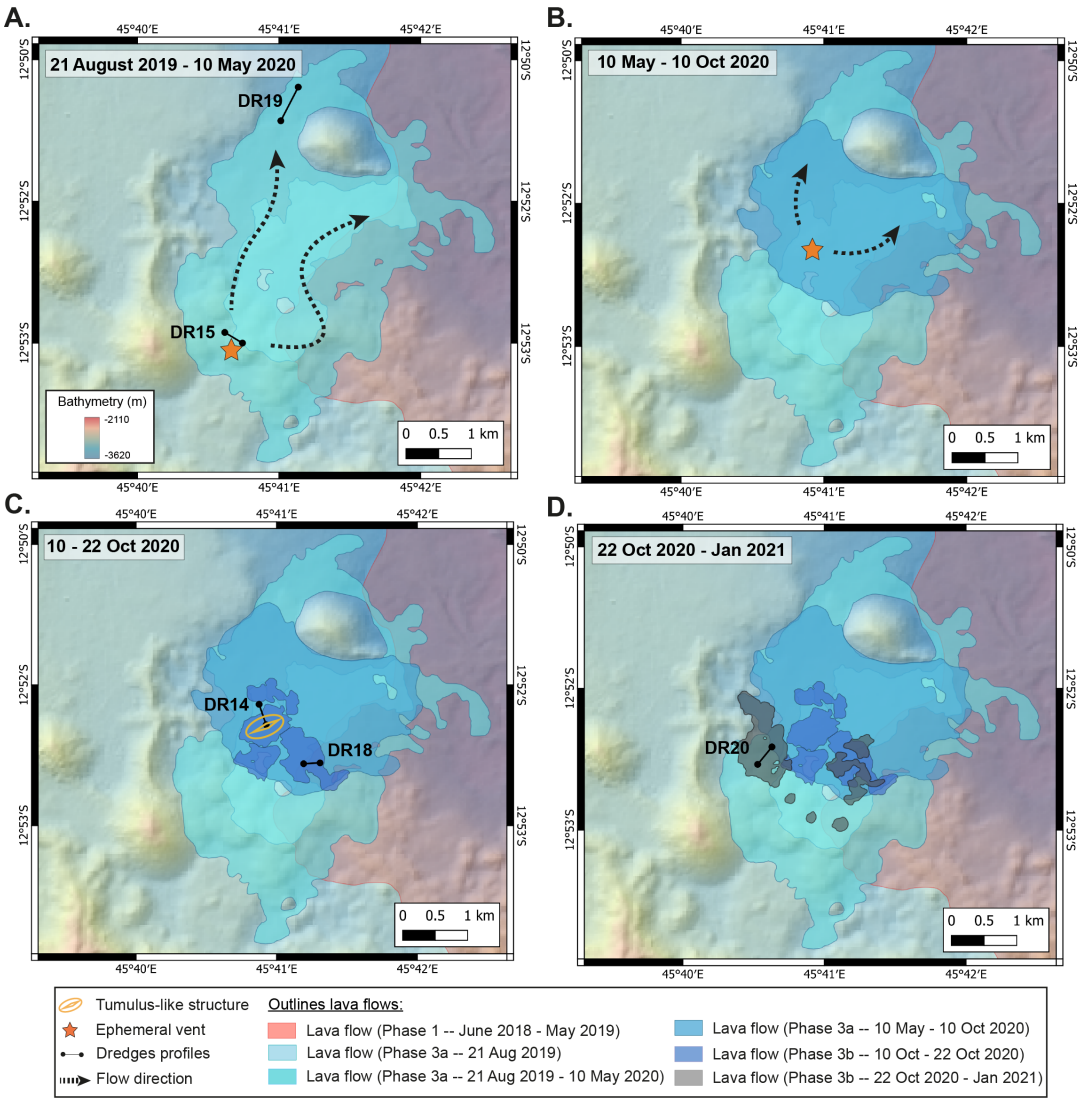

Figure 8. *Geological map showing the lava flows that took place between August 2019 and the end of the eruption in January 2021 (Phase 3a and 3b) at 6km northwest of the main volcanic cone. DR labels corresponds to the dredges.* ***A.*** *21 August 2019 – 10 May 2020* ***B.*** *10 May – 10 October 2020* ***C.*** *10 – 22 October 2020* ***D.*** *22 October 2020 – January 2021. Background is the bathymetry from MAYOBS (Rinnert, 2019). The star symbol represents the approximate location of ephemeral vent at the tip of a tube system.*

5. Conclusions

This study provides a detailed textural analysis of lava flows erupted and emplaced during the 2018–2021 submarine eruption of Fani Maoré and how they changed with time. This submarine eruption occurred at a depth of 3300 m, and was extremely well characterized by numerous oceanographic campaigns that provided an extensive sample set. The quantification of textural parameters including porosity, pore connectivity, vesicle number density (N_V) and vesicle size distributions (VSD) reveals three different textural facies. (1) The most vesicular (average porosity of 35%) lava display unimodal VSDs, a high N_V (14–214 mm^{-3}) and are characterized by small and spherical vesicles. (2) Samples with intermediate porosities (25%) are poor in small vesicles, have VSDs shifted towards larger vesicles and low N_V (0.2–39 mm^{-3}). (3) The densest samples have the lowest porosity (14%) and are characterized by a bimodal distribution, with a dominant mode of small vesicles and still a low N_V (0–87 mm^{-3}).

These results bring valuable information on spatio-temporal degassing variations during a long-lasting submarine effusive eruption. The early phase of activity (Phase 1, June 2018 – May 2019) was associated with the rapid ascent (>3 m/s) and closed-system degassing of volatile-rich magma during transfer from the deep mantle reservoir to the seafloor (Facies 1). Distal samples collected at lava flows emitted during Phases 1 and 2, between June 2018 and July 2019, mirror a decline in effusion rate with increasing evidence of outgassing during lava

591 flow emplacement (Facies 2). During the final phase (Phase 3, August 2019 – January 2021),
592 an ephemeral vent located 6 km to the northwest emitted a more degassed magma. Extended
593 periods of residence within a lava tube distribution system and an inflated flow field led to a
594 high degree of outgassing (Facies 3). Furthermore, this study emphasizes that the emplacement
595 of lava flows during Phases 2 and 3 are not related to new vents or new dykes. Indeed, during
596 Phase 1, a large lava flow was able to expand thanks to high effusion rates and where lava tubes
597 well developed. Then lava was transported through this complex lava tube system to the front
598 of the lava flow forming new distal flows. First to the south (Phase 2) and finally to the
599 northwest (Phase 3) where a new complex lava flow field with tumuli and multiple ephemeral
600 vents was established.

601 Hence, the heterogeneous textures within the studied samples reflect diverse ascent and
602 emplacement dynamics, coupled with changes in ascent and effusion rates over time as
603 observed in subaerial effusive events. Indeed, although we see a preponderance of pillows, we
604 also observe analogs with tube-fed emplacement of tumuli and inflated sheet flow. To better
605 link volatile-rich magma ascent conditions with effusion and emplacement of the associated
606 lavas, further decompression experiments are needed focusing on H_2O–CO_2 bearing basanitic
607 melts to better constrain ascent rates. Fundamentally, we find strong evidence that variations in
608 ascent rate and degassing conditions directly influence effusion rates and the style of effusive
609 eruptions on the seafloor.

610

611 ## CRediT authorship contribution statement

612 Pauline Verdurme: Investigation, Resources, Visualization, Writing - original draft. Lucia
613 Gurioli: Validation, Supervision, Funding acquisition, Investigation, Writing – review &
614 editing. Oryaëlle Chevrel: Supervision, Funding acquisition, Investigation, Writing – review &
615 editing. Etienne Médard: Supervision, Funding acquisition, Investigation, Writing – review &

editing. Carole Berthod: Supervision, Investigation, Writing – review & editing. Jean-Christophe Komorowski: Validation, Writing – review & editing. Andrew Harris: Investigation, Writing – review & editing. Fabien Paquet: Resources. Cécile Cathalot: Resources. Nathalie Feuillet: Resources, Writing – review & editing. Elodie Lebas: Resources, Writing – review & editing. Emmanuel Rinnert: Resources. Jean-Pierre Donval: Resources. Isabelle Thinon: Resources, Writing – review & editing. Christine Deplus: Resources, Writing – review & editing. Patrick Bachèlery: Writing – review & editing.

Declaration of competing interest

The authors declare that they have no known competing financial interests or personal relationships that could have appeared to influence the work reported in this paper.

Acknowledgements

MAYOBS 1 campaign was funded by the CNRS-INSU TELLUS MAYOTTE program (SISMAYOTTE project). MAYOBS 1, 2, 4, 15 and 21 campaigns were conducted by several French research institutions and laboratories (IPGP/CNRS/BRGM/IFREMER/IPGS), as part of the MAYOBS set of campaigns (https://doi.org/10.18142/291). We thank the captains and crews of the R/V Marion Dufresne (TAAF/IFREMER/LDA) and R/V *Pourquoi Pas?* (GENAVIR/IFREMER, SHOM) for their assistance. E. Rinnert, N. Feuillet, I. Thinon, E. Lebas, and F. Paquet thank their fellow mission chiefs, Y. Fouquet and S. Jorry, on the MAYOBS and GeoFlamme oceanographic campaigns. We also thank additional scientists onboard the MAYOBS cruises that conducted the dredge operations and processed the samples (M. Bickert, A. Le Friant). We thank A. Peltier (OVPF-IPGP) and C. Mucig (BRGM Mayotte)

639 respectively the Operational Leader and Co-leader of the REVOSIMA. We thank the scientists
640 of the REVOSIMA consortium for access to data and for discussions during the Scientific and
641 Technical Committee meetings. Since June 2019, all activities on Mayotte are funded by le
642 ministère de l'Enseignement Supérieur, de la Recherche et de l'Innovation (MESRI), le
643 Ministère de la Transition Ecologique (MTE), le Ministère des Outremers (MOM), le Ministère
644 de l'Intérieur (MI), and le Ministère des Armées with the support of the DIRMOM (Direction
645 Interministérielle aux Risques Majeurs en Outremer) and the MAPPPROM (Mission d'appui
646 aux politiques publiques pour la prévention des risques majeurs en Outremer). We thank the
647 IPGP for general funding to the Observatoires Volcanologiques et Sismologiques (OVS). The
648 data contributes to the Service National d'Observation en Volcanologie (SNOV). The authors
649 would like to thank IFREMER for their welcome during the sampling and E. Humler for his
650 support and national funding coordination (CNRS, REVOSIMA). The authors thank the
651 following people for their help and technical assistance: Emmy Voyer (scanning electron
652 microscopy), Lucas Delmas and Baptiste Bancharel (pycnometry measurements on DR03,
653 DR04 and DR05). The authors thank Karoly Nemeth and William W. Chadwick, whose
654 constructive reviews significantly improved the quality of the manuscript. This is contribution
655 n°644 of the ClerVolc program of the International Research Center for Disaster Sciences and
656 Sustainable Development of the University Clermont Auvergne.

657

658 References Cited

659 Berthod, C., Komorowski, J.-C., Gurioli, L., Médard, E., Bachèlery, P., Besson, P., Verdurme,
660 P., Chevrel, O., Di Muro, A., Peltier, A., Devidal, J.-L., Nowak, S., Thinon, I., Burckel, P., Hidalgo, S.,
661 Deplus, C., Loubrieu, B., Pierre, D., Bermell, S., Pitel-Roudaut, M., Réaud, Y., Fouchard, S., Bickert,
662 M., Le Friant, A., Paquet, F., Feuillet, N., Jorry, S.L., Fouquet, Y., Rinnert, E., Cathalot, C., Lebas, E.,
663 2022. Temporal magmatic evolution of the Fani Maoré submarine eruption 50 km east of Mayotte
664 revealed by in situ sampling and petrological monitoring. Comptes Rendus Géoscience 354, 1–29.
665 https://doi.org/10.5802/crgeos.155

Berthod, C., Médard, E., Bachèlery, P., Gurioli, L., Di Muro, A., Peltier, A., Komorowski, J.-C., Benbakkar, M., Devidal, J.-L., Langlade, J., Besson, P., Boudon, G., Rose-Koga, E., Deplus, C., Le Friant, A., Bickert, M., Nowak, S., Thinon, I., Burckel, P., Hidalgo, S., Kaliwoda, M., Jorry, S.J., Fouquet, Y., Feuillet, N., 2021. The 2018-ongoing Mayotte submarine eruption: Magma migration imaged by petrological monitoring. Earth Planet. Sci. Lett. 571, 117085. https://doi.org/10.1016/j.epsl.2021.117085

Blower, J., Keating, J.P., Mader, H., Phillips, J.C., 2003. The evolution of bubble size distributions in volcanic eruptions. J. Volcanol. Geotherm. Res. 120, 1–23. https://doi.org/10.1016/S0377-0273(02)00404-3

Burgisser, A., Degruyter, W., 2015. Magma Ascent and Degassing at Shallow Levels, in: The Encyclopedia of Volcanoes. Elsevier, pp. 225–236. https://doi.org/10.1016/B978-0-12-385938-9.00011-0

Buso, R., Laporte, D., Schiavi, F., Cluzel, N., Fonquernie, C., 2022. High-pressure homogenization of olivine-hosted CO_2-rich melt inclusions in a piston cylinder: insight into the volatile content of primary mantle melts. Eur. J. Mineral. 34, 325–349. https://doi.org/10.5194/ejm-34-325-2022

Calvari, S., Pinkerton, H., 1998. Formation of lava tubes and extensive flow field during the 1991-1993 eruption of Mount Etna. J. Geophys. Res. 103, 27291–27301. https://doi.org/10.1029/97JB03388

Caress, D.W., Clague, D.A., Paduan, J.B., Martin, J.F., Dreyer, B.M., Chadwick, W.W., Denny, A., Kelley, D.S., 2012. Repeat bathymetric surveys at 1-metre resolution of lava flows erupted at Axial Seamount in April 2011. Nat. Geosci. 5, 483–488. https://doi.org/10.1038/ngeo1496

Cashman, K.V., Mangan, M.T., Newman, S., 1994. Surface degassing and modifications to vesicle size distributions in active basalt flows. J. Volcanol. Geotherm. Res. 61, 45–68. https://doi.org/10.1016/0377-0273(94)00015-8

Chadwick, W.W., Cashman, K.V., Embley, R.W., Matsumoto, H., Dziak, R.P., de Ronde, C.E.J., Lau, T.K., Deardorff, N.D., Merle, S.G., 2008. Direct video and hydrophone observations of submarine explosive eruptions at NW Rota-1 volcano, Mariana arc: submarine explosive eruptions at NW Rota-1. J. Geophys. Res. Solid Earth 113. https://doi.org/10.1029/2007JB005215

Chavrit, D., Humler, E., Grasset, O., 2014. Mapping modern CO_2 fluxes and mantle carbon content all along the mid-ocean ridge system. Earth Planet. Sci. Lett. 387, 229–239. https://doi.org/10.1016/j.epsl.2013.11.036

Chavrit, D., Humler, E., Morizet, Y., Laporte, D., 2012. Influence of magma ascent rate on carbon dioxide degassing at oceanic ridges: Message in a bubble. Earth Planet. Sci. Lett. 357–358, 376–385. https://doi.org/10.1016/j.epsl.2012.09.042

Colombier, M., Vasseur, J., Houghton, B.F., Cáceres, F., Scheu, B., Kueppers, U., Thivet, S., Gurioli, L., Montanaro, C., Soldati, A., Di Muro, A., Dingwell, D.B., 2021. Degassing and gas percolation in basaltic magmas. Earth Planet. Sci. Lett. 573, 117134. https://doi.org/10.1016/j.epsl.2021.117134

Colombier, M., Wadsworth, F.B., Gurioli, L., Scheu, B., Kueppers, U., Di Muro, A., Dingwell, D.B., 2017. The evolution of pore connectivity in volcanic rocks. Earth Planet. Sci. Lett. 462, 99–109. https://doi.org/10.1016/j.epsl.2017.01.011

Cooper, A.F., Adam, L.J., Coulter, R.F., Eby, G.N., McIntosh, W.C., 2007. Geology, geochronology and geochemistry of a basanitic volcano, White Island, Ross Sea, Antarctica. J. Volcanol. Geotherm. Res. 165, 189–216. https://doi.org/10.1016/j.jvolgeores.2007.06.003

Crisp, J.A., 1984. Rates of magma emplacement and volcanic output. J. Volcanol. Geotherm. Res. 20, 177–211. https://doi.org/10.1016/0377-0273(84)90039-8

Dixon, J., Clague, D.A., Wallace, P.J., Poreda, R.J., 1997. Volatiles in Alkalic Basalts form the North Arch Volcanic Field, Hawaii: Extensive Degassing of Deep Submarine-erupted Alkalic Series Lavas. J. Petrol. 38, 911–939.

Feuillet, N., Jorry, S., Crawford, W.C., Deplus, C., Thinon, I., Jacques, E., Saurel, J.M., Lemoine, A., Paquet, F., Satriano, C., Aiken, C., Foix, O., Kowalski, P., Laurent, A., Rinnert, E., Cathalot, C., Donval, J.-P., Guyader, V., Gaillot, A., Scalabrin, C., Moreira, M., Peltier, A., Beauducel, F., Grandin, R., Ballu, V., Daniel, R., Pelleau, P., Gomez, J., Besançon, S., Geli, L., Bernard, P., Bachelery, P., Fouquet, Y., Bertil, D., Lemarchand, A., Van der Woerd, J., 2021. Birth of a large volcanic edifice offshore Mayotte via lithosphere-scale dyke intrusion. Nat. Geosci. 14, 787–795. https://doi.org/10.1038/s41561-021-00809-x

Feuillet, N., 2019. MAYOBS1 cruise, Marion Dufresne R/V. https://doi.org/10.17600/18001217

Fornari, D.J., 1986. Submarine lava tubes and channels. Bull. Volcanol. 48, 291–298. https://doi.org/10.1007/BF01081757

Fouquet, Y., Feuillet, N., 2019. MAYOBS4 cruise, Marion Dufresne R/V. https://doi.org/10.17600/18001238

Giachetti, T., Druitt, T.H., Burgisser, A., Arbaret, L., Galven, C., 2010. Bubble nucleation, growth and coalescence during the 1997 Vulcanian explosions of Soufrière Hills Volcano, Montserrat. J. Volcanol. Geotherm. Res. 193, 215–231. https://doi.org/10.1016/j.jvolgeores.2010.04.001

Graham, D.W., Michael, P.J., Rubin, K.H., 2018. An investigation of mid-ocean ridge degassing using He, CO_2, and $\delta^{13}C$ variations during the 2005–06 eruption at 9°50′N on the East Pacific Rise. Earth Planet. Sci. Lett. 504, 84–93. https://doi.org/10.1016/j.epsl.2018.09.040

Gregg, T., Fink, J., 1995. Quantification of submarine lava-flow morphology through analog experiments. Geology 23. https://doi.org/10.1130/0091-7613(1995)023<0073:QOSLFM>2.3.CO;2

Gudmundsson, A., 2002. Emplacement and arrest of sheets and dykes in central volcanoes. J. Volcanol. Geotherm. Res. 116, 279–298. https://doi.org/10.1016/S0377-0273(02)00226-3

Gurioli, L., Di Muro, A., 2017. DynVolc Database: Datasets Collection composed by textural and chemical data from volcano eruption. https://doi.org/10.25519/DYNVOLC-DATABASE

Gurioli, L., Harris, A.J.L., Houghton, B.F., Polacci, M., Ripepe, M., 2008. Textural and geophysical characterization of explosive basaltic activity at Villarrica volcano: activity characterization at Villarrica. J. Geophys. Res. Solid Earth 113. https://doi.org/10.1029/2007JB005328

Harris, A.J.L., Dehn, J., Calvari, S., 2007. Lava effusion rate definition and measurement: a review. Bull. Volcanol. 70, 1–22. https://doi.org/10.1007/s00445-007-0120-y

Harris, A.J.L., Rowland, S.K., 2015. Lava Flows and Rheology, in: The Encyclopedia of Volcanoes. Elsevier, pp. 321–342. https://doi.org/10.1016/B978-0-12-385938-9.00017-1

Harris, A.J.L., Rowland, S.K., Chevrel, M.O., 2022. The anatomy of a channel-fed ‘a‘ā lava flow system. Bull. Volcanol. 84, 70. https://doi.org/10.1007/s00445-022-01578-0

Head, E.M., Shaw, A.M., Wallace, P.J., Sims, K.W.W., Carn, S.A., 2011. Insight into volatile behavior at Nyamuragira volcano (D.R. Congo, Africa) through olivine-hosted melt inclusions: volatile

behavior at Nyamuragira volcano. Geochem. Geophys. Geosystems 12, n/a-n/a. https://doi.org/10.1029/2011GC003699

Hekinian, R., Chaigneau, M., Cheminee, J.L., 1973. Popping Rocks and Lava Tubes from the Mid-Atlantic Rift Valley at 36° N. Nature 245, 371–373. https://doi.org/10.1038/245371a0

Hekinian, R., Pineau, F., Shilobreeva, S., Bideau, D., Gracia, E., Javoy, M., 2000. Deep sea explosive activity on the Mid-Atlantic Ridge near 34°50′N: Magma composition, vesicularity and volatile content. J. Volcanol. Geotherm. Res. 98, 49–77. https://doi.org/10.1016/S0377-0273(99)00190-0

Hon, K., Kauahikaua, J., Denlinger, R., Mackay, K., 1994. Emplacement and inflation of pahoehoe sheet flows: Observations and measurements of active lava flows on Kilauea Volcano, Hawaii. Geol. Soc. Am. Bull. 106, 351–370. https://doi.org/10.1130/0016-7606(1994)106<0351:EAIOPS>2.3.CO;2

Hudgins, T.R., Mukasa, S.B., Simon, A.C., Moore, G., Barifaijo, E., 2015. Melt inclusion evidence for CO_2-rich melts beneath the western branch of the East African Rift: implications for long-term storage of volatiles in the deep lithospheric mantle. Contrib. Mineral. Petrol. 169, 46. https://doi.org/10.1007/s00410-015-1140-9

James, M.R., Lane, S.J., Corder, S.B., 2008. Modelling the rapid near-surface expansion of gas slugs in low-viscosity magmas. Geol. Soc. Lond. Spec. Publ. 307, 147–167. https://doi.org/10.1144/SP307.9

Jones, M.R., Soule, S.A., Gonnermann, H.M., Le Roux, V., Clague, D.A., 2018. Magma ascent and lava flow emplacement rates during the 2011 Axial Seamount eruption based on CO_2 degassing. Earth Planet. Sci. Lett. 494, 32–41. https://doi.org/10.1016/j.epsl.2018.04.044

Jones, M.R., Wanless, V.D., Soule, S.A., Kurz, M.D., Mittelstaedt, E., Fornari, D.J., Curtice, J., Klein, F., Le Roux, V., Brodsky, H., Péron, S., Schwartz, D.M., 2019. New constraints on mantle carbon from Mid-Atlantic Ridge popping rocks. Earth Planet. Sci. Lett. 511, 67–75. https://doi.org/10.1016/j.epsl.2019.01.019

Jorry, S., 2019. MAYOBS2 cruise, Marion Dufresne R/V. https://doi.org/10.17600/18001222

Keszthelyi, L., 1995. Measurements of the cooling at the base of Pahoehoe Flows. Geophys. Res. Lett. 22, 2195–2198. https://doi.org/10.1029/95GL01812

Lavayssière, A., Retailleau, L., 2023. Capturing Mayotte's deep magmatic plumbing system and its spatiotemporal evolution with volcano-tectonic seismicity. Volcanica 6, 331–344. https://doi.org/10.30909/vol.06.02.331344

Le Gall, N., Pichavant, M., 2016a. Homogeneous bubble nucleation in H_2O- and H_2O-CO_2-bearing basaltic melts: Results of high temperature decompression experiments. J. Volcanol. Geotherm. Res. 327, 604–621. https://doi.org/10.1016/j.jvolgeores.2016.10.004

Le Gall, N., Pichavant, M., 2016b. Experimental simulation of bubble nucleation and magma ascent in basaltic systems: Implications for Stromboli volcano. Am. Mineral. 101, 1967–1985. https://doi.org/10.2138/am-2016-5639

Lemoine, A., Briole, P., Bertil, D., Roullé, A., Foumelis, M., Thinon, I., Raucoules, D., de Michele, M., Valty, P., Hoste Colomer, R., 2020. The 2018–2019 seismo-volcanic crisis east of Mayotte, Comoros islands: seismicity and ground deformation markers of an exceptional submarine eruption. Geophys. J. Int. 223, 22–44. https://doi.org/10.1093/gji/ggaa273

Masquelet ,C., Watremez L., Leroy S., Sauter D., Delescluse M., Chamot-Rooke N., Ringenbach J.C., Thinon I.,Lemoine A. and Franke D. *(submitted* Tectonophysics*)* Intra-oceanic emplacement of the Comoros Archipelago through inherited fracture zones

Masquelet, C., Leroy, S., Delescluse, M., Chamot-Rooke, N., Thinon, I., Lemoine, A., Franke, D., Watremez, L., Werner, P., Paquet, F., Berthod, C., Cabiativa Pico, V., Sauter, D., 2022. The East-Mayotte new volcano in the Comoros Archipelago: structure and timing of magmatic phases inferred from seismic reflection data. Comptes Rendus Géoscience 354, 1–15. https://doi.org/10.5802/crgeos.154

Mattox, T.N., Heliker, C., Kauahikaua, J., Hon, K., 1993. Development of the 1990 Kalapana Flow Field, Kilauea Volcano, Hawaii. Bull. Volcanol. 55, 407–413. https://doi.org/10.1007/BF00302000

Mercury, N., Lemoine, A., Doubre, C., Bertil, D., Van Der Woerd, J., Hoste-Colomer, R., Battaglia, J., 2023. Onset of a submarine eruption east of Mayotte, Comoros archipelago: the first ten months seismicity of the seismo-volcanic sequence (2018–2019). Comptes Rendus Géoscience 354, 105–136. https://doi.org/10.5802/crgeos.191

Mourtada-Bonnefoi, C.C., Laporte, D., 2004. Kinetics of bubble nucleation in a rhyolitic melt: an experimental study of the effect of ascent rate. Earth Planet. Sci. Lett. 218, 521–537. https://doi.org/10.1016/S0012-821X(03)00684-8

Murch, A.P., Portner, R.A., Rubin, K.H., Clague, D.A., 2022. Deep-subaqueous implosive volcanism at West Mata seamount, Tonga. Earth Planet. Sci. Lett. 578, 117328. https://doi.org/10.1016/j.epsl.2021.117328

Peltier, A., Saur, S., Ballu, V., Beauducel, F., Briole, P., Chanard, K., Dausse, D., De Chabalier, J.-B., Grandin, R., Rouffiac, P., Tranchant, Y.-T., de Berc, M.B., Besançon, S., Boissier, P., Broucke, C., Brunet, C., Canjamalé, K., Carme, E., Catherine, P., Colombain, A., Crawford, W., Daniel, R., Dectot, G., Desfete, N., Doubre, C., Dumouch, T., Griot, C., Grunberg, M., Jund, H., Kowalski, P., Lauret, F., Lebreton, J., Pesqueira, F., Tronel, F., Valty, P., van der Woerd, J., 2022. Ground deformation monitoring of the eruption offshore Mayotte. Comptes Rendus Géoscience 354, 1–23. https://doi.org/10.5802/crgeos.176

Perfit, M.R., Cann, J.R., Fornari, D.J., Engels, J., Smith, D.K., Ian Ridley, W., Edwards, M.H., 2003. Interaction of sea water and lava during submarine eruptions at mid-ocean ridges. Nature 426, 62–65. https://doi.org/10.1038/nature02032

Polacci, M., Cashman, K.V., Kauahikaua, J.P., 1999. Textural characterization of the pāhoeho–ʻaʻa transition in Hawaiian basalt. Bull. Volcanol. 60, 595–609. https://doi.org/10.1007/s004450050254

Polacci, M., Papale, P., 1997. The evolution of lava flows from ephemeral vents at Mount Etna: Insights from vesicle distribution and morphological studies. J. Volcanol. Geotherm. Res. 76, 1–17. https://doi.org/10.1016/S0377-0273(96)00070-4

REVOSIMA, 2024. Bulletin de l'activité sismo-volcanique à Mayotte du 1 au 29 Février 2024. IPGP, Université de Paris, BRGM, Ifremer. https://www.ipgp.fr/volcanoweb/mayotte/Bulletins-Communiques/Bulletins/2024/Revosima_bull_20240306.pdf. ISSN: 2680-1205

Rinnert, E., 2019. MAYOBS. https://doi.org/10.18142/291

Rinnert, E., Cathalot, C., Feuillet, N., 2021a. GeoFLAMME cruise, Pourquoi pas ? R/V. https://doi.org/10.17600/18001297

Rinnert, E., Thinon, I., Feuillet, N., 2020. MD 228 / MAYOBS15 cruise, Marion Dufresne R/V. https://doi.org/10.17600/18001745

Rinnert, E., Thinon, I., Lebas, E., 2021b. MAYOBS21 cruise, Marion Dufresne R/V. https://doi.org/10.17600/18001986

Rivalta, E., Böttinger, M., Dahm, T., 2005. Buoyancy-driven fracture ascent: Experiments in layered gelatine. J. Volcanol. Geotherm. Res. 144, 273–285. https://doi.org/10.1016/j.jvolgeores.2004.11.030

Robert, B., Harris, A., Gurioli, L., Médard, E., Sehlke, A., Whittington, A., 2014. Textural and rheological evolution of basalt flowing down a lava channel. Bull. Volcanol. 76, 824. https://doi.org/10.1007/s00445-014-0824-8

Rowland, S.K., Walker, G.P., 1990. Pahoehoe and aa in Hawaii: volumetric flow rate controls the lava structure. Bull. Volcanol. 52, 615–628. https://doi.org/10.1007/BF00301212

Sarda, P., Graham, D.W., 1990. Mid-ocean ridge popping rocks: implications for degassing at ridge crests. Earth Planet. Sci. Lett. 97, 268–289.

Schiavi, F., Bolfan-Casanova, N., Buso, R., Laumonier, M., Laporte, D., Medjoubi, K., Venugopal, S., Gómez-Ulla, A., Cluzel, N., Hardiagon, M., 2020. Quantifying magmatic volatiles by Raman microtomography of glass inclusion-hosted bubbles. Geochem. Perspect. Lett. 16, 17–24. https://doi.org/10.7185/geochemlet.2038

Shea, T., Houghton, B.F., Gurioli, L., Cashman, K.V., Hammer, J.E., Hobden, B.J., 2010. Textural studies of vesicles in volcanic rocks: An integrated methodology. J. Volcanol. Geotherm. Res. 190, 271–289. https://doi.org/10.1016/j.jvolgeores.2009.12.003

SHOM-Service Hydrographique Et Océanographique De La Marine, 2016. MNT bathymétrique de façade de Mayotte (Projet Homonim). https://doi.org/10.17183/MNT_MAY100M_HOMONIM_WGS84

Soule, S.A., Nakata, D.S., Fornari, D.J., Fundis, A.T., Perfit, M.R., Kurz, M.D., 2012. CO2 variability in mid-ocean ridge basalts from syn-emplacement degassing: Constraints on eruption dynamics. Earth Planet. Sci. Lett. 327–328, 39–49. https://doi.org/10.1016/j.epsl.2012.01.034

Taisne, B., Jaupart, C., 2009. Dike propagation through layered rocks. J. Geophys. Res. 114, B09203. https://doi.org/10.1029/2008JB006228

Thivet, S., Gurioli, L., Di Muro, A., 2020. Basaltic dyke eruptions at Piton de La Fournaise: characterization of the eruptive products with implications for reservoir conditions, conduit processes and eruptive dynamics. Contrib. Mineral. Petrol. 175, 26. https://doi.org/10.1007/s00410-020-1664-5

Thivet, S., Hess, K.-U., Dingwell, D.B., Berthod, C., Gurioli, L., Di Muro, A., Lacombe, T., Komorowski, J.-C., 2023a. Volatiles of the active Mayotte volcanic chain: STA & EGA-MS analysis of volcanic products. Chem. Geol. 618, 121297. https://doi.org/10.1016/j.chemgeo.2022.121297

Thivet, S., Pereira, L., Menguy, N., Médard, É., Verdurme, P., Berthod, C., Troadec, D., Hess, K.-U., Dingwell, D.B., Komorowski, J.-C., 2023b. Metastable liquid immiscibility in the 2018–2021 Fani Maoré lavas as a mechanism for volcanic nanolite formation. Commun. Earth Environ. 4, 483. https://doi.org/10.1038/s43247-023-01158-w

Toramaru, A., 2006. BND (bubble number density) decompression rate meter for explosive volcanic eruptions. J. Volcanol. Geotherm. Res. 154, 303–316. https://doi.org/10.1016/j.jvolgeores.2006.03.027

877 Verdurme, P., Le Losq, C., Chevrel, O., Pannefieu, S., Médard, E., Berthod, C., Komorowski,
878 J.-C., Bachèlery, P., Neuville, D.R., Gurioli, L., 2023. Viscosity of crystal-free silicate melts from the
879 active submarine volcanic chain of Mayotte. Chem. Geol. 121326.
880 https://doi.org/10.1016/j.chemgeo.2023.121326

881 Walker, G.P.L., 1991. Structure, and origin by injection of lava under surface crust, of
882 tumuli, lava rises, lava-rise pits, and lava-inflation clefts in Hawaii. Bull. Volcanol. 53, 546–558.
883 https://doi.org/10.1007/BF00298155

884 Walker, G.P.L., 1989. Spongy pahoehoe in Hawaii: A study of vesicle-distribution patterns in
885 basalt and their significance. Bull. Volcanol. 51, 199–209. https://doi.org/10.1007/BF01067956

886 Watson, E.B., Sneeringer, M.A., Ross, A., 1982. Diffusion of dissolved carbonate in magmas:
887 Experimental results and applications. Earth Planet. Sci. Lett. 61, 346–358.
888 https://doi.org/10.1016/0012-821X(82)90065-6

889 Wilmoth, R.A., Walker, G.P.L., 1993. P-type and S-type pahoehoe: a study of vesicle
890 distribution patterns in Hawaiian lava flows. J. Volcanol. Geotherm. Res. 55, 129–142.
891 https://doi.org/10.1016/0377-0273(93)90094-8

892 Yoshimura, S., 2015. Diffusive fractionation of H_2O and CO_2 during magma degassing. Chem.
893 Geol. 411, 172–181. https://doi.org/10.1016/j.chemgeo.2015.07.003

894